Model-Based Iterative Reconstruction for Dual-Energy X-Ray CT Using a Joint Quadratic Likelihood Model

Ruoqiao Zhang*, *Student Member, IEEE*, Jean-Baptiste Thibault, *Member, IEEE*, Charles A. Bouman, *Fellow, IEEE*, Ken D. Sauer, *Member, IEEE*, and Jiang Hsieh, *Senior Member, IEEE*

***Abstract*—Dual-energy X-ray CT (DECT) has the potential to improve contrast and reduce artifacts as compared to traditional CT. Moreover, by applying model-based iterative reconstruction (MBIR) to dual-energy data, one might also expect to reduce noise and improve resolution. However, the direct implementation of dual-energy MBIR requires the use of a nonlinear forward model, which increases both complexity and computation. Alternatively, simplified forward models have been used which treat the material-decomposed channels separately, but these approaches do not fully account for the statistical dependencies in the channels. In this paper, we present a method for joint dual-energy MBIR (JDE-MBIR), which simplifies the forward model while still accounting for the complete statistical dependency in the material-decomposed sinogram components. The JDE-MBIR approach works by using a quadratic approximation to the polychromatic log-likelihood and a simple but exact nonnegativity constraint in the image domain. We demonstrate that our method is particularly effective when the DECT system uses fast kVp switching, since in this case the model accounts for the inaccuracy of interpolated sinogram entries. Both phantom and clinical results show that the proposed model produces images that compare favorably in quality to previous decomposition-based methods, including FBP and other statistical iterative approaches.**

***Index Terms*—Computed tomography (CT), dual-energy CT (DECT), model-based iterative reconstruction (MBIR), spectral CT, statistical reconstruction.**

I. Introduction

DUAL-ENERGY computed tomography (DECT) scanners, which acquire X-ray projections with two distinct spectra, are of great interest in applications such as medical imaging [1], [2], security inspection [3], [4], and nondestructive testing [5]. The objective of DECT reconstruction is to determine the energy-dependent attenuation at each voxel. Fortunately, for most materials, the energy-dependent attenuation is accurately approximated as a linear combination of two basis functions corresponding to photoelectric absorption and Compton scattering [6]. In practice, it is usually more convenient to reparameterize the energy-dependent attenuation as a linear combination of two basis materials or components [7] such as water and iodine. So in this case, our objective is then to accurately reconstruct cross sections corresponding to the equivalent densities of, say, water and iodine.

Early work on dual-energy reconstruction focused on decomposing the dual-energy measurements into two independent sinograms, each of which corresponds to a basis component or material. This can be done by first applying a material-decomposition function to the two energy measurements. This material-decomposition function then produces two sinograms corresponding to the two basis materials. Many methods have been proposed over the years for experimentally determining this function. Alvarez and Macovski [6] proposed the numerical inversion of a polynomial approximation to the polychromatic measurement process. Other approaches directly approximate the material-decomposition function as a polynomial [7]–[12], or compute the decomposition through an iterative estimation process [4], [13]–[15].

Alternatively, other approaches to dual-energy reconstruction work by first reconstructing images from the low- and high-energy sinograms using filtered back projection (FBP) method, and then performing image-domain material decomposition [16]–[19]. However, while sometimes effective, this type of image-domain reconstruction makes substantial approximations, particularly when the X-ray spectrum for each measurement is broad. So the resulting reconstructions may be quantitatively inaccurate and suffer from artifacts. Recently, an iterative FBP method [20] has been proposed to account for the polychromatic spectra. It repeats the process that performs back projection, image-domain material decomposition, and forward projection of the decomposed results with a calibrated nonlinear model. This method can be applied to the case where one of the dual-energy measurements is missing for each ray.

Recently, statistical reconstruction based on iterative methods has been found to be very effective in single-energy CT reconstruction [21]–[24]; and in particular, model-based iterative reconstruction (MBIR) methods [21], [24]–[26], which incorporate an accurate system model, statistical noise model, and prior

Manuscript received July 10, 2013; revised September 02, 2013; accepted September 09, 2013. Date of publication September 17, 2013; date of current version December 27, 2013. This work was supported by GE Healthcare. *Asterisk indicates corresponding author.*

*R. Zhang is with the School of Electrical and Computer Engineering, Purdue University, West Lafayette, IN 47907 USA (e-mail: zhang393@purdue.edu).

J.-B. Thibault and J. Hsieh are with GE Healthcare Technologies, Waukesha, WI 53188 USA (e-mail: jean-baptiste.thibault@med.ge.com; jiang.hsieh@med.ge.com).

C. A. Bouman is with the School of Electrical and Computer Engineering, Purdue University, West Lafayette, IN 47907 USA (e-mail: bouman@ecn.purdue.edu).

K. D. Sauer is with the Department of Electrical Engineering, University of Notre Dame, Notre Dame, IN 46556 USA (e-mail: sauer@nd.edu).

Color versions of one or more of the figures in this paper are available online at http://ieeexplore.ieee.org.

Digital Object Identifier 10.1109/TMI.2013.2282370

model, have demonstrated the ability to reduce noise and improve resolution [27]–[31].

Several statistical iterative approaches have been proposed for DECT reconstruction. These methods can be mainly classified into two categories, the direct-inversion methods and the decomposition-based methods. The direct-inversion methods reconstruct images directly from dual-energy measurements [32]–[36]. In particular, Fessler *et al.* [33] formulated the likelihood function of the detector output by using a Poisson model. Huh and Fessler [35] applied a penalized weighted least square (PWLS) approach to DECT with fast kVp switching acquisition and used an approximate Gaussian noise model for the log-transformed measurements. These approaches generally include a highly nonlinear forward model in the likelihood function to model the polychromatic measurement process, so this formulation increases complexity and consequently complicates the optimization.

Alternatively, decomposition-based statistical approaches reconstruct images from material-decomposed sinograms [37]–[39] with a simplified forward model. Fessler *et al.* [37], [39] applied PWLS approaches with diagonal weighting matrices for the pair of decomposed sinogram entries. These methods, which we refer to as independent dual-energy MBIR (independent DE-MBIR), model the decomposed sinogram entries as statistically independent when conditioned on image content. The independent DE-MBIR methods are computationally simpler than the direct-inversion methods, but the decoupled likelihood functions ignore the correlation in sinogram entries that are caused by the decomposition process [40], [41]. Perhaps the most closely related work is Kinahan, Alessio, and Fessler's [38] method for dual-energy PWLS reconstruction in PET/CT attenuation correction. This framework also allowed for the potential correlation of sinogram entries, but left open the specifics of how the entries should be weighted.

In this paper, we develop a novel joint dual-energy MBIR (JDE-MBIR) method to reconstruct basis material densities from the decomposed sinograms. In Section II-C, we introduce a key novelty of the JDE-MBIR method, which is a quadratic approximation to the joint likelihood model. This quadratic approximation weights the decomposed sinogram entries by nondiagonal matrices that explicitly model the noise correlation in the decomposition domain. The proposed method also incorporates a prior model that accounts for the separation into materials and introduces a simple but exact nonnegativity constraint that accurately reflects the true physical constraint of nonnegative X-ray attenuation. We use the iterative coordinate descent (ICD) algorithm to compute the solution. We note that a preliminary version of this method was presented in the conference paper of [42].

An important novelty of JDE-MBIR is that it achieves computational efficiency by reconstructing from material-decomposed sinograms while retaining an accurate forward model and noise model in the decomposition domain. In particular, the JDE-MBIR models the interdependence in decomposed sinogram entries that result from the decomposition process. This model leads to reconstructions with less noise than those of the independent DE-MBIR methods.

The JDE-MBIR also allows for accurate modeling of DECT data collected using fast kVp switching techniques. Fig. 1 illustrates a model for the fast kVp switching technique, in which the system alternates between low- and high-energy measurements from view to view. In this case, each view contains either low- or high-energy measurements, whereas the material decomposition requires both to be available. Although the angular difference between the low- and high-energy measurements is small, an additional interpolation step needs to be performed for the traditional decomposition-based approaches to ensure perfect registration. The JDE-MBIR method also exploits sinogram interpolation; however, the reconstruction principally depends on only the real measurements, which makes it robust to interpolation error and capable of preserving more resolution than other decomposition-based approaches.

We also propose a novel nonnegativity constraint for the DECT reconstruction. Previous approaches have enforced nonnegativity constraints directly on reconstructed material densities [32], [35], [43], which is not generally physically correct. We proposed a nonnegativity constraint that is applied in the attenuation space. This constraint can be enforced as two simple linear constraints on the material images and accurately reflects the true physical constraints of X-ray attenuation.

In our experiments, we evaluate the performance of the JDE-MBIR by using phantom and clinical data. The experimental results show that the JDE-MBIR significantly improves resolution and reduces noise in the reconstructed material density images and the synthesized monochromatic images.

The paper is organized as follows. Section II describes the formulation of the JDE-MBIR. Section III gives the ICD solution to the optimization problem. Section IV presents the experimental results on phantom and clinical data to demonstrate the image quality improvement achieved by JDE-MBIR as compared to FBP and independent DE-MBIR.

II. MAP Reconstruction Framework

Let $y \in \Re^{M\times 2}$ be the set of dual-energy CT measurements, where each row, $y_i = [y_{i,\mathrm{l}}, y_{i,\mathrm{h}}]$, specifies the low- and high-energy projection measurements for the ith ray. We use subscript "l" for "low-energy" and subscript "h" for "high-energy." Furthermore, let $m \in \Re^{N\times 2}$ be the reconstructed density images of the scanned object for the selected material basis pair, where each row, $m_j = [m_{j,\mathrm{W}}, m_{j,\mathrm{I}}]$, represents the water- and iodine-equivalent densities for the jth voxel. We use subscript "W" for "water" and subscript "I" for "iodine." In this paper, we choose water and iodine since they are frequently used as basis materials for separation into low and high X-ray attenuation characteristics, respectively. However, the use of other material pairs is equally valid. The integer M specifies the number of distinct ray paths during data acquisition, and N specifies the number of voxels in the reconstructed volume.

Our goal is to reconstruct the material density images, m, from the measurements, y. One typical approach is to compute the maximum *a posteriori* (MAP) estimate of m given by

$$\hat{m} = \arg\max_{m\in\Omega} \{\log P(y|m) + \log P(m)\} \qquad (1)$$

where $P(y|m)$ is the conditional distribution of y given m, $P(m)$ is the prior distribution of m, and Ω is the constraint set for the reconstruction.

The following sections develop the theoretical framework for the JDE-MBIR algorithm from the basic physical models. Section II-A presents a noise model for the dual-energy detector measurements based on photon statistics. Section II-B then derives the forward model for the dual-energy data using widely accepted models of polychromatic X-ray attenuation through materials. With this framework in place, Section II-C then introduces the primary innovation of our technique, which is a quadratic approximation to the log-likelihood function in the projection domain. Section II-D then shows how this innovative model can be applied to the important problem of fast kVp switching data and provides a theoretical analysis of JDE-MBIR's advantages in this application.

A. Measurement Preprocessing

In the X-ray transmission problem, we measure the photon flux after object attenuation, which is denoted by $\lambda_{i,k}$ for ray i and source spectrum k, where $k \in \{\mathrm{l}, \mathrm{h}\}$. We also measure the air scan photon flux, $\lambda_{i,k,0}$, which counts the detected photons with no object present. The air scan counts can be calibrated accurately by repeated scans and therefore are assumed noiseless. The projection measurement, y_i, is then computed as the negative log of the photon measurement normalized by the corresponding air scan photon count

$$\begin{aligned} y_i &= [y_{i,\mathrm{l}}, y_{i,\mathrm{h}}] \\ &\triangleq \left[-\log\left(\frac{\lambda_{i,\mathrm{l}}}{\lambda_{i,\mathrm{l},0}}\right), -\log\left(\frac{\lambda_{i,\mathrm{h}}}{\lambda_{i,\mathrm{h},0}}\right)\right]. \end{aligned} \tag{2}$$

We model $\lambda_{i,k}$ as the summation of a Poisson random variable with conditional mean $\bar{\lambda}_{i,k}$ and a Gaussian random variable with mean zero and variance σ_e^2. In fact, $\bar{\lambda}_{i,k}$ is the conditional mean of $\lambda_{i,k}$ given the image m, and the Gaussian random variable presents additive electronic noise in the detector system. From this, the conditional mean and variance of $\lambda_{i,k}$ are given by

$$\mathrm{E}[\lambda_{i,k}|m] = \bar{\lambda}_{i,k} \tag{3}$$

$$\mathrm{Var}(\lambda_{i,k}|m) = \bar{\lambda}_{i,k} + \sigma_e^2. \tag{4}$$

Then we approximate the conditional mean of $y_{i,k}$ as

$$\mathrm{E}[y_{i,k}|m] \cong -\log\left(\frac{\bar{\lambda}_{i,k}}{\lambda_{i,k,0}}\right). \tag{5}$$

To compute the conditional variance of $y_{i,k}$, we first perform a first-order Taylor series expansion to the expression of $y_{i,k}$ in (2) about $\bar{\lambda}_{i,k}$

$$\begin{aligned} y_{i,k} &= -\log\left(\frac{\lambda_{i,k}}{\lambda_{i,k,0}}\right) \\ &\cong -\log\left(\frac{\bar{\lambda}_{i,k}}{\lambda_{i,k,0}}\right) - \frac{1}{\bar{\lambda}_{i,k}}(\lambda_{i,k} - \bar{\lambda}_{i,k}) \\ &\cong \mathrm{E}[y_{i,k}|m] - \frac{1}{\bar{\lambda}_{i,k}}(\lambda_{i,k} - \bar{\lambda}_{i,k}) \end{aligned} \tag{6}$$

which yields the approximation we will use for the conditional variance of $y_{i,k}$ [44]

$$\mathrm{Var}(y_{i,k}|m) \cong \frac{\mathrm{Var}(\lambda_{i,k}|m)}{\bar{\lambda}_{i,k}^2} = \frac{\bar{\lambda}_{i,k} + \sigma_e^2}{\bar{\lambda}_{i,k}^2} \cong \frac{\lambda_{i,k} + \sigma_e^2}{\lambda_{i,k}^2} \tag{7}$$

where $\bar{\lambda}_{i,k}$ is approximated by its observation, $\lambda_{i,k}$. Thus, we will model the conditional mean and covariance of y_i as

$$\mathrm{E}[y_i|m] = [\mathrm{E}[y_{i,\mathrm{l}}|m], \mathrm{E}[y_{i,\mathrm{h}}|m]] \tag{8}$$

$$\mathrm{Cov}(y_i|m) = \begin{bmatrix} \mathrm{Var}(y_{i,\mathrm{l}}|m) & 0 \\ 0 & \mathrm{Var}(y_{i,\mathrm{h}}|m) \end{bmatrix}. \tag{9}$$

Note that the off-diagonal elements of the covariance matrix are zeros since we assume that the low- and high-energy measurements are made independently.

Assuming y_i is conditionally Gaussian with mean and covariance given by (8) and (9), the distribution of y_i is given by

$$-\log P(y_i|m) = \frac{1}{2}\left(y_i - \mathrm{E}[y_i|m]\right) W_i \left(y_i - \mathrm{E}[y_i|m]\right)^T + C \tag{10}$$

where C is a normalizing constant, and W_i is the inverse covariance of y_i

$$W_i = \begin{bmatrix} w_{i,\mathrm{l}} & 0 \\ 0 & w_{i,\mathrm{h}} \end{bmatrix} \triangleq \mathrm{Cov}^{-1}(y_i|m) \tag{11}$$

where

$$w_{i,\mathrm{l}} = \frac{1}{\mathrm{Var}(y_{i,\mathrm{l}}|m)} \cong \frac{\lambda_{i,\mathrm{l}}^2}{\lambda_{i,\mathrm{l}} + \sigma_e^2} \tag{12}$$

$$w_{i,\mathrm{h}} = \frac{1}{\mathrm{Var}(y_{i,\mathrm{h}}|m)} \cong \frac{\lambda_{i,\mathrm{h}}^2}{\lambda_{i,\mathrm{h}} + \sigma_e^2}. \tag{13}$$

With the assumption of measurements at distinct projections being conditionally independent, the distribution of the data given the object information is given by

$$-\log P(y|m) = \frac{1}{2}\sum_{i=1}^{M}\left(y_i - \mathrm{E}[y_i|m]\right) W_i \left(y_i - \mathrm{E}[y_i|m]\right)^T + C. \tag{14}$$

However, this function is still a nonlinear function of m because the conditional expectation, $\mathrm{E}[y_i|m]$, is in general a nonlinear function of the argument m. In Section II-C, we will use this result to construct a fully quadratic approximation to the log-likelihood in (14).

B. Forward Model

We next need to formulate a physical model for $\mathrm{E}[y_i|m]$. Given the linear attenuation coefficients, μ, the conditional mean of $\lambda_{i,k}$ is computed by integrating the photon attenuation over the source spectrum

$$\mathrm{E}[\lambda_{i,k}|\mu] = \bar{\lambda}_{i,k} = \int_{\Re} \lambda_{i,k,0} S_k(\mathcal{E}) e^{-\int_{\mathrm{ray}_i} \mu(r,\mathcal{E})\mathrm{d}r} \mathrm{d}\mathcal{E} \tag{15}$$

where $\mathcal{E}$ (keV) is the photon energy, $S_k(\mathcal{E})$ is the normalized photon energy distribution for source spectrum k, and $\mu(r, \mathcal{E})$

(cm^{-1}) is the linear attenuation coefficient as a function of location r and energy $\mathcal{E}$, representing X-ray photon absorption per unit distance. Since μ and m contain the same information, note that $\mathrm{E}[\cdot|\mu] = \mathrm{E}[\cdot|m]$.

If we discretize $\mu(r, \mathcal{E})$, then this leads to the expression

$$\mathrm{E}[\lambda_{i,k}|\mu] = \int_{\Re} \lambda_{i,k,0} S_k(\mathcal{E}) e^{-\sum_{j=1}^{N} A_{i,j}\mu_j(\mathcal{E})} \mathrm{d}\mathcal{E} \tag{16}$$

where $A \in \Re^{M\times N}$ is the projection matrix, with its element, $A_{i,j}$ (cm), representing the intersection of ray i with voxel j. We use the distance driven approach [45] to compute A. Then from (5), the conditional mean of the projection measurement is given by

$$\mathrm{E}[y_i|\mu] = -\log\left(\int_{\Re} S(\mathcal{E}) e^{-\sum_{j=1}^{N} A_{i,j}\mu_j(\mathcal{E})} \mathrm{d}\mathcal{E}\right) \tag{17}$$

where $y_i = [y_{i,\mathrm{l}}, y_{i,\mathrm{h}}]$ and $S(\mathcal{E}) = [S_{\mathrm{l}}(\mathcal{E}), S_{\mathrm{h}}(\mathcal{E})]$.

Moreover, the linear attenuation coefficient can be expressed as a linear combination of the mass attenuation functions of two or more basis materials [7]. With water and iodine as the basis, the linear attenuation function can be decomposed as

$$\mu_j(\mathcal{E}) = m_{j,\mathrm{W}}\varphi_{\mathrm{W}}(\mathcal{E}) + m_{j,\mathrm{I}}\varphi_{\mathrm{I}}(\mathcal{E}) \tag{18}$$

where $m_{j,s}$ $(\mathrm{mg/cm}^3)$ is the equivalent density for basis material s at voxel j, where $s \in \{\mathrm{W}, \mathrm{I}\}$, and $\varphi_s(\mathcal{E})$ $(\mathrm{cm}^2/\mathrm{mg})$ is the known energy-dependent mass attenuation function for basis material s, which represents the photon absorption per unit distance for the particular material with 100% concentration under standard temperature and pressure. Note that the reconstructions, $m_{j,\mathrm{W}}$ and $m_{j,\mathrm{I}}$, do not depend on energy.

Then, by substituting (18) into (17), we have

$$\begin{aligned}
&\mathrm{E}[y_i|m] \\
&\quad = -\log\left(\int_{\Re} S(\mathcal{E}) e^{-\sum_{j=1}^{N} A_{i,j}(m_{j,\mathrm{W}}\varphi_{\mathrm{W}}(\mathcal{E}) + m_{j,\mathrm{I}}\varphi_{\mathrm{I}}(\mathcal{E}))} \mathrm{d}\mathcal{E}\right) \\
&\quad \triangleq -\log\left(\int_{\Re} S(\mathcal{E}) e^{-p_i(\varphi(\mathcal{E}))^T} \mathrm{d}\mathcal{E}\right)
\end{aligned} \tag{19}$$

where $\varphi(\mathcal{E}) \triangleq [\varphi_{\mathrm{W}}(\mathcal{E}), \varphi_{\mathrm{I}}(\mathcal{E})]$, and p_i $(\mathrm{mg/cm}^2)$ is the material density projection defined as

$$p_i \triangleq [p_{i,\mathrm{W}}, p_{i,\mathrm{I}}] \triangleq \left[\sum_{j=1}^{N} A_{i,j} m_{j,\mathrm{W}}, \sum_{j=1}^{N} A_{i,j} m_{j,\mathrm{I}}\right] \triangleq [Am]_i. \tag{20}$$

The quantity p_i represents the line integral of material densities along ray i. We then define a vector-valued function, $h : \Re^2 \to \Re^2$, as

$$h(p_i) \triangleq -\log\left(\int_{\Re} S(\mathcal{E}) e^{-p_i(\varphi(\mathcal{E}))^T} \mathrm{d}\mathcal{E}\right) \tag{21}$$

which models the nonlinear relationship between the material density projections and the expected photon attenuation. From this, we have

$$\mathrm{E}[y_i|m] = h\left([Am]_i\right). \tag{22}$$

The function h does not depend on particular ray paths generally; however, it can be a function of the ray index, i, if the source spectrum, $S(\mathcal{E})$, varies among rays. This is the case in practice with systems including bowtie filters to shape the X-ray beam to a particular scanned object.

Thus, substituting (22) into (14), we have the negative log-likelihood function

$$\begin{aligned}
&-\log P(y|m) \\
&\quad = \frac{1}{2}\sum_{i=1}^{M} \left(y_i - h\left([Am]_i\right)\right) W_i \left(y_i - h\left([Am]_i\right)\right)^T + C.
\end{aligned} \tag{23}$$

This is the likelihood function used in the direct-inversion methods.

While the forward model of (23) could be used directly for MBIR reconstruction, it is not practical for a number of reasons. First, the function h is generally not measured on real CT systems. In practice, real CT systems require a knowledge of the material decomposition function, h^{-1}, as described in the following section. This is because h^{-1} is required for implementation of standard direct reconstruction methods such as FBP; so it is accurately measured using calibration procedures. However, h is not easily computed from h^{-1} and would require a completely separate calibration procedure. Second, direct nonlinear optimization of the MAP cost function using (23) would be very complex and potentially very computationally expensive since it does not have a quadratic form. So our goal will next be to derive a quadratic function that accurately approximates (23).

C. Quadratic Joint Likelihood Model

In this section, we introduce a quadratic approximation to the negative log-likelihood function, $-\log P(y|m)$, which reduces the complexity of the reconstruction algorithm while still retaining an accurate model of the noise correlation in the decomposition domain.

We first define the inverse function, $h^{-1} : \Re^2 \to \Re^2$, as

$$h^{-1}\left(h(p_i)\right) \triangleq p_i. \tag{24}$$

In practice, the h^{-1} function is called the "material decomposition function." There are a variety of means to determine this function. One may employ a polynomial approximation to the h function and then solve numerically for p_i [6], or directly approximate the h^{-1} function as a polynomial [7]–[12]. The coefficients of the polynomial approximations can be determined empirically by system calibration. Possible calibration methods include a projection-domain calibration [11], [46], or an image-domain approach [12]. One may also compute the decomposition through an iterative estimation process [4], [13]–[15]. In practice, we approximate the h^{-1} function as a high order polynomial through calibration, which will be described in detail in Section IV.

With the h^{-1} function, we can then compute the decomposed sinogram entries, $\hat{p}_i = [\hat{p}_{i,\mathrm{W}}, \hat{p}_{i,\mathrm{I}}]$, as

$$\hat{p}_i \triangleq h^{-1}(y_i) \tag{25}$$

with $\hat{p}_i$ an estimate of the material density projection, p_i. Performing a Taylor series expansion of $[Am]_i$ at y_i yields

$$\begin{aligned}[Am]_i &= h^{-1}\left(h\left([Am]_i\right)\right) \\ &\cong h^{-1}(y_i) + \left(h\left([Am]_i\right) - y_i\right)\left[\nabla h^{-1}(y_i)\right] \\ &= \hat{p}_i + \left(h\left([Am]_i\right) - y_i\right)\left[\nabla h^{-1}(y_i)\right] \end{aligned} \tag{26}$$

where $\nabla h^{-1}(y_i)$ is the gradient of function h^{-1} at y_i. For our problem, $\nabla h^{-1}(y_i)$ is a 2×2 invertible matrix. This results in the linear approximation we will use in the model

$$y_i - h\left([Am]_i\right) \cong \left(\hat{p}_i - [Am]_i\right)\left[\nabla h^{-1}(y_i)\right]^{-1}. \tag{27}$$

Thus, by substituting (27) into (23), we approximate the true log-likelihood function in (23) by

$$-\log P(y|m) \cong \frac{1}{2}\sum_i \left(\hat{p}_i - [Am]_i\right) B_i \left(\hat{p}_i - [Am]_i\right)^T + C' \tag{28}$$

where the estimated material projection, $\hat{p}_i$, is given by (25), and the statistical weighting matrix, B_i, is given by

$$B_i \triangleq \left[\nabla h^{-1}(y_i)\right]^{-1} W_i \left[\nabla h^{-1}(y_i)\right]^{-T}. \tag{29}$$

Each B_i is a 2×2 symmetric matrix representing the inverse covariance of the decomposed sinogram entries, $\hat{p}_i$. Each B_i is therefore also positive semi-definite and has a zero eigenvalue if and only if the diagonal matrix, W_i, has a zero eigenvalue, which implies that $\lambda_{i,\mathrm{l}} = 0$ in (12) or $\lambda_{i,\mathrm{h}} = 0$ in (13).

The (28) gives the likelihood model we use in the proposed JDE-MBIR method. In contrast to the direct-inversion methods, our model has a simple quadratic form, so it allows for direct application of existing quadratic optimization methods for the computation of the MAP reconstruction.

It should also be noted that our weighting matrix, B_i, is in general nondiagonal for every projection. The off-diagonal elements of B_i provide significant information about the noise correlation between distinct decomposed sinogram entries.

D. Likelihood Model for Fast kVp Switching Modality

Our proposed model is particularly well suited for CT systems that use fast kVp switching to acquire dual-energy data. Fig. 1 graphically illustrates a model for the fast kVp switching technique, in which the system alternates between low- and high-energy measurements between adjacent views. Fast kVp switching requires high-speed detectors and X-ray sources and generators that allow for fast switching, but it offers the advantage that low- and high-energy measurements are interlaced closely in time and space so that misalignments due to motion or other effects are minimized. Notice that a fast kVp switching system has the capability of varying the duty cycle between low- and high-energy views to optimize dose. This is graphically depicted by the fact that the low-energy (orange) line may be longer than the high-energy (green) line. For typical scans, the low-energy dwell time is greater than the high-energy dwell

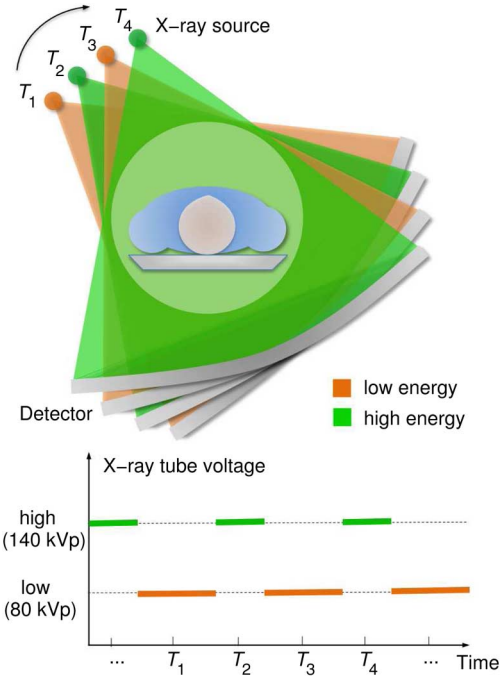

Fig. 1. This figure illustrates a model for fast kVp switching technique. Single X-ray tube alternates the voltage between low- and high-kVp from view to view. Thus, each view contains only one measurement, either low- or high-energy.

time, but this depends on many details of the scan parameters. While the dwell time may be different from view to view, data acquisition still results in consecutive views alternating between low- and high-energy measurements. Dwell time characteristics are taken into account in h^{-1} by calibration. The dwell time of the view generally will affect the resulting noise variance, with longer dwell times reducing noise variance and short ones increasing variance. However, this change in variance is fully accounted for by the estimates of noise variance given in Section II-A and more specifically by (7).

For fast kVp switching, each projection contains either low- or high-energy measurements. Therefore, for each projection, either $y_{i,\mathrm{l}}$ or $y_{i,\mathrm{h}}$ is missing. In the case of the true likelihood of (23), this missing measurement can be accommodated by setting the weighting matrix to be

$$W_i = \begin{cases} \begin{bmatrix} w_{i,\mathrm{l}} & 0 \\ 0 & 0 \end{bmatrix}, & \text{for low-energy projections} \\ \begin{bmatrix} 0 & 0 \\ 0 & w_{i,\mathrm{h}} \end{bmatrix}, & \text{for high-energy projections.} \end{cases} \tag{30}$$

So in this case, the missing measurement is always weighted by zero.

However, in the case of the joint approximation in (28), we still must determine a value for the weighting matrix B_i from (29) and the estimated projection, $\hat{p}_i$, from (25). Unfortunately, both these values depend on the missing measurement. In order to solve this problem, we interpolate the missing value of y_i, and use this interpolated value to compute both the gradient of h^{-1} used for the weight matrix B_i, and the projection $\hat{p}_i$. While this interpolation process does introduce error, this error is relatively minor when the joint log-likelihood approximation

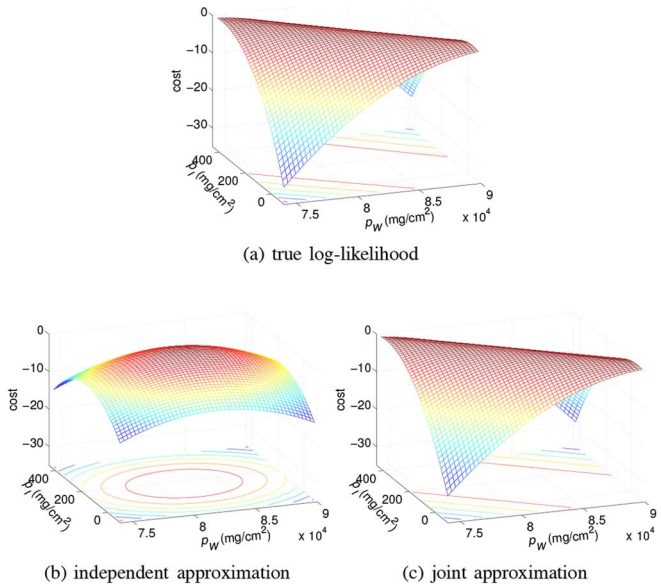

(a) true log-likelihood

(b) independent approximation (c) joint approximation

Fig. 2. Plots of the true log-likelihood function, the independent approximation, and the proposed joint approximation, with contours plotted underneath.

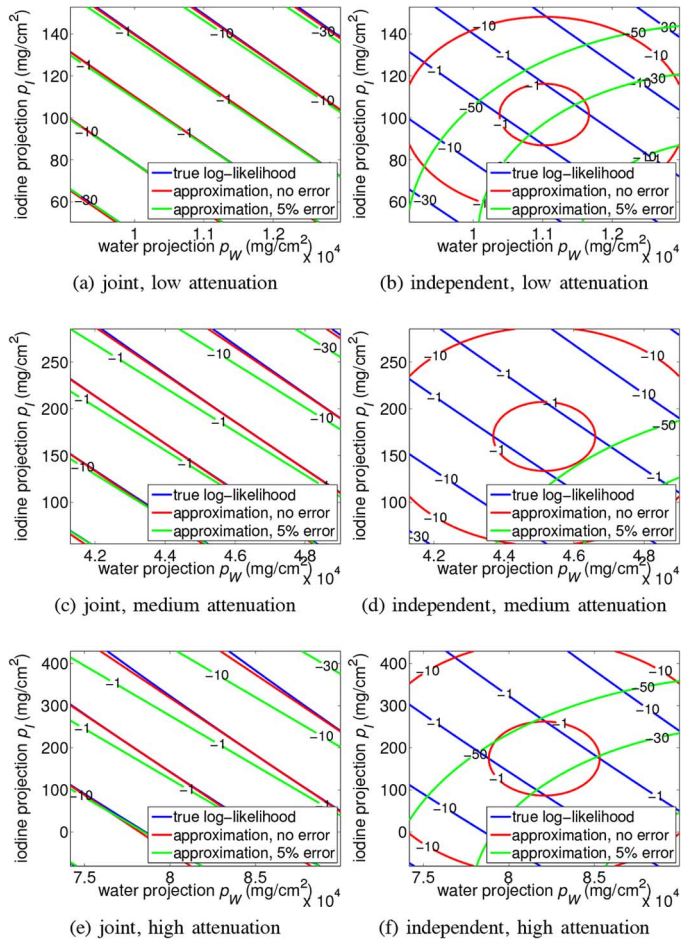

(a) joint, low attenuation (b) independent, low attenuation

(c) joint, medium attenuation (d) independent, medium attenuation

(e) joint, high attenuation (f) independent, high attenuation

Fig. 3. This figure plots the contours of the true log-likelihood function and different approximations. We compare the independent model and the joint model within three different attenuation levels. Within each figure, we plot the contours of the true log-likelihood (blue), approximation without interpolation error (red), and same approximation with 5% interpolation error present (green). Without loss of generality, we fix the air scan photon flux to be $[\lambda_{1,0}, \lambda_{\mathrm{h},0}] = [5000, 5000]$, and then simulate the low, medium, and high attenuation cases with photon measurements $[\lambda_{\mathrm{l}}, \lambda_{\mathrm{h}}]$ equivalent to [2500,2650], [500,550], and [100, 110], respectively. Each plot covers two standard deviations of water and iodine projections.

is used, which allows using relatively straightforward interpolation techniques without significant concern for the quality of the reconstructed images. In order to see this, consider the plots of Figs. 2 and 3.

Fig. 2 graphically illustrates the importance of using the joint log-likelihood approximation rather than the simplified independent approximation using some typical values of $[y_{i,\mathrm{l}}, y_{i,\mathrm{h}}] = [3.9, 3.8]$ at 80 and 140 kVp. In the independent approximation, the off-diagonal entries of B_i are set to zero, so the errors in $\hat{p}_{i,\mathrm{W}}$ and $\hat{p}_{i,\mathrm{I}}$ are modeled as independent, and the approximated log-likelihood function has ellipsoidal level curves. This is a very poor approximation of the true log-likelihood and artificially imposes a penalty for any deviation from its unique maximum. With incorporation of the off-diagonal terms in B_i, the joint approximation is much more accurate. The joint approximation appropriately retains the under-specified nature of the maximum-likelihood projection estimate, allowing it to move along its level lines without change in cost.

Fig. 3 illustrates more precisely the effect of interpolation error in the joint and independent log-likelihood approximations. The figure shows contour plots of the log-likelihood function of Fig. 2, but also shows the effect of a 5% interpolation error in the missing sample. The interpolation error has a relatively minor effect on the joint approximation, while shifting quite significantly the maximum of the independent model. Intuitively, the joint approximation is very robust to interpolation error because the weighting matrix, B_i, has a zero eigenvalue in the direction of any interpolation error. This is due to the fact that the underlying matrix W_i of (29) has a zero in the location of the missing sample. In practice, we will see that the independent approximation results in reconstructions which lose resolution due to the interpolation process. Alternatively, the joint approximation approach preserves resolution by primarily depending on only the uninterpolated samples in the reconstruction.

Fig. 4 provides a pseudocode of the joint log-likelihood approximation for fast kVp switching. First, the missing measurement is interpolated, and then the interpolated value is used to compute the material decomposition estimate, $\hat{p}_i$, and the projection weighting matrix, B_i.

E. Prior Model

We model the reconstructed density image as a Markov random field (MRF) with the following form:

$$-\log P(m) = \sum_{s\in\{\mathrm{W},\mathrm{I}\}} \sum_{\{j,r\}\in\mathcal{C}} b_{jr,s}\rho_s(m_{j,s} - m_{r,s}) \qquad (31)$$

where s is the index of material type, $\{j, r\}$ specifies a neighboring pair consisting of voxel j and voxel r, $\mathcal{C}$ represents the set of all such voxel pairs, $b_{jr,s}$ is the prior strength for voxel pair $\{j, r\}$ and material s, and $\rho(.)$ is the potential function. We choose $b_{jr,s}$ to be inversely proportional to the distance between

JDE-MBIR$(y_{\rm l}, y_{\rm h}, w_{\rm l}, w_{\rm h}, h^{-1}, \nabla h^{-1})\{$
for $i = 1$ to M **do**
  if $w_{i,\rm h} = 0$ **then**
    $y_{i,\rm h} \leftarrow$ Interpolation
  else if $w_{i,\rm l} = 0$ **then**
    $y_{i,\rm l} \leftarrow$ Interpolation
  end if
  $y_i \leftarrow [y_{i,\rm l},\ y_{i,\rm h}]$
  $W_i \leftarrow diag\{w_{i,\rm l},\ w_{i,\rm h}\}$
  $\hat{p}_i \leftarrow h^{-1}(y_i)$ {*Material decomposition*}
  $B_i \leftarrow [\nabla h^{-1}(y_i)]^{-1} W_i [\nabla h^{-1}(y_i)]^{-T}$
end for
$\hat{m} \leftarrow$ ImageRecon$(\hat{p}, B)$
return $\hat{m}$
$\}$

Fig. 4. Pseudocode of JDE-MBIR for DECT that uses fast kVp switching. First, we interpolate the missing sample for each projection. Second, we perform material decomposition and also compute the statistical weighting matrix. Finally, we use the decomposed sinograms and weighting matrices to reconstruct the images iteratively. Subroutine ImageRecon is described in Fig. 8.

voxel j and voxel r, and the scale of $b_{jr,s}$ can be further adjusted to balance between noise and resolution in the reconstruction. By choosing this model, we perform the regularization independently on each of the material components in the image domain.

Our particular choice of potential function is the q-generalized Gaussian MRF (q-GGMRF) of the form

$$\rho_s(\Delta) = \frac{|\Delta|^p}{1 + |\Delta/c_s|^{p-q}} \tag{32}$$

with $1 < q \leq p \leq 2$. This type of prior has shown to be effective in many tomographic reconstruction studies [21], [24], [47]–[49]. With $1 < q \leq p \leq 2$, the potential function is strictly convex [21], which guarantees global convergence of the cost function and produces reconstruction as a continuous function of the data [50].

We set $p = 2.0$ and $q = 1.2$ in our application, since this particular setting has shown a desirable compromise between noise and resolution in similar clinical studies [21]. With $p = 2.0$, the potential approximates a quadratic function for small voxel differences, which preserves details in low contrast regions. The value, $q = 1.2$, approximates the behavior of a generalized Gaussian MRF [50] for large voxel differences, which preserves edges in high contrast regions. The parameter c models the transition between low and high contrast contents. In practice, we choose $c_{\rm W} = 10$ mg/cm^3 for water image and $c_{\rm I} = 0.5$ mg/cm^3 for iodine image.

F. Constrained Optimization

In X-ray tomographic reconstruction problems, an important physical constraint to the reconstruction is that the linear attenuation of any material at any photon energy must be nonnegative. More precisely, for all $\mathcal{E} \in [40, 140]$ keV, we know that

$$\mu_j(\mathcal{E}) = m_j \cdot \varphi(\mathcal{E}) \geq 0 \tag{33}$$

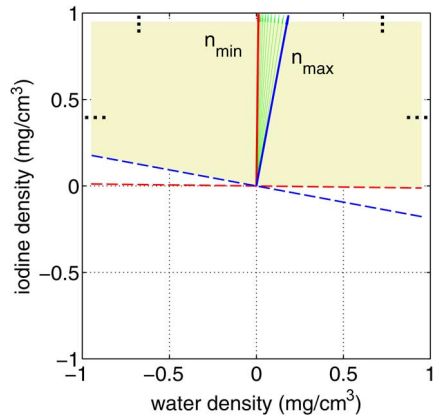

Fig. 5. This figure illustrates the feasible values of a voxel, $m_j = [m_{j,\rm W}, m_{j,\rm I}]$, where $m_{j,\rm W}$ is the water-equivalent density and $m_{j,\rm I}$ is the iodine-equivalent density. Yellow region shows the constrained solution set, which is formed by the intersection of only two half planes, one defined by $n_{\max}$ and the other by $n_{\min}$. Green arrows show the attenuation vectors at intermediate energies.

where the photon energy range [40, 140] keV is of particular interest for medical imaging and is above the k-edge of iodine.

Let Ω' be the constraint set of a single voxel value, as

$$\Omega' = \cap_{\mathcal{E}\in[40,140]} \left\{ m_j \in \Re^2 : m_j \cdot n(\mathcal{E}) \geq 0 \right\} \tag{34}$$

where $n(\mathcal{E}) \triangleq \varphi(\mathcal{E})/\|\varphi(\mathcal{E})\|$ is the normalized mass attenuation vector. In this way, Ω' is formed by the intersection of an infinite number of half planes. However, the form of Ω' can be dramatically simplified by observing that the direction of $n(\mathcal{E})$ moves continuously with $\mathcal{E}$. As a consequence, the constraint can be represented much more simply by the intersection of only two planes corresponding to the minimum and maximum values of $n(\mathcal{E})$, as $n_{\min} = n(40)$ and $n_{\max} = n(140)$

$$\Omega' = \{ m_j \in \Re^2 : m_j \cdot n_{\min} \geq 0 \text{ and } m_j \cdot n_{\max} \geq 0 \}. \tag{35}$$

Fig. 5 illustrates the constraint set and the associated mass attenuation vectors. Then the constraint set for the entire image, denoted by Ω, is given by

$$\Omega = {\Omega'}^N \tag{36}$$

where N is the number of voxels in the reconstructed volume. Clearly, Ω' is a convex set and so is Ω.

The proposed constraint allows negative values for the reconstructed densities of water and iodine. This is because the reconstructed densities are only some coefficients for the linear combination that produces the equivalent attenuation. However, in the attenuation domain, the combination of the reconstructed material densities should remain nonnegative.

Combining the log-likelihood in (28) and the prior in (31) with the constraints in (36) yields the expression for the MAP reconstruction of (1)

$$\hat{m} = \arg\min_{m\in\Omega} \left\{ \frac{1}{2} \sum_{i=1}^{M} (\hat{p}_i - [Am]_i)\, B_i\, (\hat{p}_i - [Am]_i)^T + \sum_{s\in\{\rm W,I\}} \sum_{\{j,r\}\in\mathcal{C}} b_{jr,s} \rho(m_{j,s} - m_{r,s}) \right\}. \tag{37}$$

III. Optimization Algorithm

There are a wide variety of techniques that can be used to solve the optimization problem in (37), from which we choose the iterative coordinate descent (ICD) algorithm. The ICD algorithm has the advantages that it has rapid convergence at high spatial frequencies [25], especially when initialized with FBP to obtain a good original estimate of low frequencies. Moreover, it can easily incorporate the proposed nonnegativity constraint.

The ICD algorithm sequentially updates voxels of the reconstructed image. Within each ICD iteration, every single voxel is updated with remaining voxels fixed so as to minimize the total cost function. Within each ICD update, we compute the exact solution to the constrained voxel update with the Karush–Kuhn–Tucker (KKT) condition.

More precisely, by changing only one voxel while fixing the rest of the image, we compute the voxel update, $\hat{m}_j$, from the current image, m, by

$$\hat{m}_j \leftarrow \arg\min_{u\in\Omega'} \left\{ \frac{1}{2}\sum_{i=1}^{M} \|\hat{p}_i - [Am]_i + A_{i,j}(m_j - u)\|^2_{B_i} + \sum_{s\in\{\mathrm{W},\mathrm{I}\}} \sum_{r\in\partial j} b_{jr,s}\rho(u_s - m_{r,s}) \right\}. \quad (38)$$

We denote $\|x\|^2_B = xBx^T$ for simplicity. We introduce a dummy variable $u = [u_{\mathrm{W}}, u_{\mathrm{I}}]$ to represent the voxel value being updated, to distinguish from its current value, m_j. Define the error sinogram, $e \triangleq Am - \hat{p}$. Then intuitively, the first term in (38) describes the change in the error sinogram introduced by the change in the voxel value. Equivalently, (38) can be written as

$$\hat{m}_j \leftarrow \arg\min_{u\in\Omega'} \left\{ (u - m_j)\theta_1 + \frac{1}{2}\|u - m_j\|^2_{\theta_2} + \sum_{s\in\{\mathrm{W},\mathrm{I}\}} \sum_{r\in\partial j} b_{jr,s}\rho(u_s - m_{r,s}) + const. \right\} \quad (39)$$

where θ_1 and θ_2 are the first and second derivatives of the log-likelihood function, which are given by

$$\theta_1 \triangleq \sum_{i=1}^{M} A_{i,j}B_i e_i^T \quad (40)$$

$$\theta_2 \triangleq \sum_{i=1}^{M} A_{i,j}^2 B_i \quad (41)$$

where $e_i = [Am]_i - \hat{p}_i$ is the ith row of the error sinogram, and $A_{i,j}$ is a scalar representing the intersection of ray i with voxel j.

Solving the 2-D optimization problem in (39) simultaneously for both material components may be difficult, since the prior term cannot be explicitly expressed as a function of u. To address this problem, one may use a functional substitution approach [24], [51]–[54]. In this problem, we introduce a quadratic substitute function for the potential function. More precisely, let $\Delta = u_s - m_{r,s}$ and $\Delta^* = m_{j,s} - m_{r,s}$. Then we define the substitute function, $q(\Delta;\Delta^*)$, as

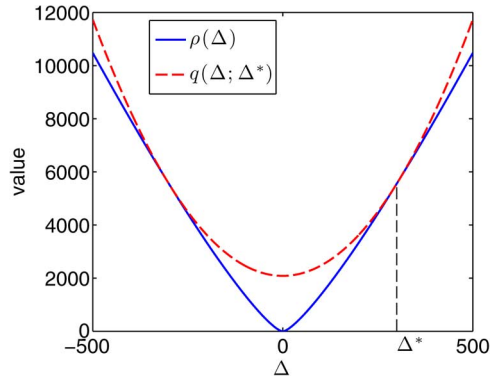

Fig. 6. This figure illustrates the desired substitute function. The substitute function, $q(\Delta;\Delta^*)$, equals the true function, $\rho(\Delta)$, at $\Delta = \Delta^*$, and upper bounds the true function everywhere else. Thus, the true function is guaranteed to decrease when the substitute function is minimized.

$$q(\Delta;\Delta^*) = \frac{\alpha_{jr,s}}{2}\Delta^2 + C_{jr,s} \quad (42)$$

with

$$\alpha_{jr,s} = \frac{\rho'(\Delta^*)}{\Delta^*}$$
$$C_{jr,s} = \rho(\Delta^*) - \frac{\rho'(\Delta^*)}{2}\Delta^* \quad (43)$$

where $C_{jr,s}$ is an offset constant and therefore can be ignored during optimization. This function, $q(\Delta;\Delta^*)$, satisfies the following two constraints for a valid substitute function [24], [51]–[53]

$$q(\Delta^*;\Delta^*) = \rho(\Delta^*)$$
$$q(\Delta;\Delta^*) \geq \rho(\Delta).$$

Intuitively, a valid substitute function for minimization should equal the true function at the current point and upper bound the true function everywhere else. Fig. 6 illustrates the desired substitute function, $q(\Delta;\Delta^*)$. It is important to know that replacing the true potential function with the substitute function still guarantees monotone convergence of the cost function [24], [53].

Replacing the potential function in (39) with the substitute function yields a quadratic cost function of u

$$\hat{m}_j \leftarrow \arg\min_{u\in\Omega'} \left\{ (u - m_j)\theta_1 + \frac{1}{2}\|u - m_j\|^2_{\theta_2} + \frac{1}{2}\sum_{r\in\partial j} \|u - m_r\|^2_{\psi_r} + const. \right\} \quad (44)$$

where

$$\psi_r \triangleq \begin{bmatrix} b_{jr,\mathrm{W}}\alpha_{jr,\mathrm{W}} & 0 \\ 0 & b_{jr,\mathrm{I}}\alpha_{jr,\mathrm{I}} \end{bmatrix}. \quad (45)$$

KKTSolve($\phi_1, \phi_2, n_{\min}, n_{\max}$){
  // *unconstrained solution*
  $u \leftarrow -\phi_2^{-1}\phi_1$
if $u \cdot n_{\min} < 0$ **or** $u \cdot n_{\max} < 0$ **then**
  // *solve on the boundary defined by* $u \cdot n_{\min} = 0$
  $u^T \leftarrow -\left(\phi_2^{-1} - \frac{\phi_2^{-1} n_{\min}^T n_{\min} \phi_2^{-1}}{n_{\min}\phi_2^{-1} n_{\min}^T}\right)\phi_1$
  $\lambda_1 \leftarrow \frac{n_{\min}^T \phi_2^{-1}\phi_1}{n_{\min}\phi_2^{-1} n_{\min}^T}$
  if $u \cdot n_{\max} < 0$ **or** $\lambda_1 \le 0$ **then**
    // *solve on the boundary defined by* $u \cdot n_{\max} = 0$
    $u^T \leftarrow -\left(\phi_2^{-1} - \frac{\phi_2^{-1} n_{\max}^T n_{\max} \phi_2^{-1}}{n_{\max}\phi_2^{-1} n_{\max}^T}\right)\phi_1$
    $\lambda_2 \leftarrow \frac{n_{\max}^T \phi_2^{-1}\phi_1}{n_{\max}\phi_2^{-1} n_{\max}^T}$
    if $u \cdot n_{\min} < 0$ **or** $\lambda_2 \le 0$ **then**
      // *only feasible solution is the origin*
      $u \leftarrow [0, 0]$
    end if
  end if
end if
return u
}

Fig. 7. Pseudocode for solving the quadratic minimization problem in (48) with the KKT condition. We first test the KKT condition on the unconstrained solution. If it fails, we solve the minimization problem on either boundary of the feasible set, and then we test the corresponding solution with the KKT condition. Once the KKT condition is met, the particular solution becomes the updated value. Origin will be the only feasible solution if no qualified solution is found in the previous cases. Derivation for the solution is provided in the Appendix.

ImageRecon($\hat{p}, B$){
  $m \leftarrow$ raw FBP images
  $A \leftarrow$ Compute
  $e \leftarrow Am - \hat{p}$
  $n_{\min}, n_{\max} \leftarrow$ Compute
repeat
  repeat
    $j \leftarrow$ Select a voxel according to random schedule
    $A_{*,j} \leftarrow$ Compute
    $\theta_1, \theta_2 \leftarrow$ Compute by using (40) and (41)
    for each $r \in \partial j$ **do**
      $\psi_r \leftarrow$ Compute by using (43) and (45)
    end for
    $\phi_1, \phi_2 \leftarrow$ Compute by using (46) and (47)
    $\hat{m}_j \leftarrow$ KKTSolve($\phi_1, \phi_2, n_{\min}, n_{\max}$)
    $e \leftarrow e + A_{*,j}(\hat{m}_j - m_j)$
    $m \leftarrow m + \delta_j(\hat{m}_j - m_j)$
  until All voxels have been visited
until Image m converges to the desired level
return m
}

Fig. 8. Pseudocode for reconstructing the image by using generic ICD algorithm. We initialize m with the raw FBP images and also initialize the error sinogram. Within each iteration, for each selected voxel, we first compute the column of the forward projection matrix. Second, we compute first two derivatives of the log-likelihood function. Third, we compute the coefficients for the surrogate prior. Fourth, we compute the first two derivatives of the quadratic cost function. Fifth, we solve the optimization problem with the KKT condition to obtain the voxel update. Finally, we update the error sinogram and the image. We define δ_j as an $N \times 1$ vector that is 1 for element j and 0 otherwise. Subroutine KKTSolve is described in Fig. 7.

Furthermore, define

$$\phi_1 \triangleq \theta_1 - \theta_2 m_j^T - \sum_{r \in \partial j} \psi_r m_r^T \tag{46}$$

$$\phi_2 \triangleq \theta_2 + \sum_{r \in \partial j} \psi_r. \tag{47}$$

By using ϕ_1 and ϕ_2, we rewrite (44) into a standard form

$$\begin{aligned} \min_{u} \quad & \frac{1}{2} u \phi_2 u^T + u\phi_1 + const. \\ \text{s.t.} \quad & u \cdot n_{\min} \ge 0 \\ & u \cdot n_{\max} \ge 0. \end{aligned} \tag{48}$$

This is a standard quadratic minimization problem with two linear constraints. It can be solved exactly by applying the KKT condition following a standard procedure [55]. Fig. 7 shows the procedure for computing the solution. We first test the KKT condition on the unconstrained solution. If it fails, we solve the minimization problem on either boundary of the feasible set by rooting the derivative of the resulting 1-D cost function, and then test the corresponding solution with the KKT condition. Once the KKT condition is met, the particular solution becomes our updated value. This is because the KKT condition is both necessary and sufficient in this problem, given that the cost function and the constraints are continuously differentiable and convex [56]. The origin will be the only feasible solution if no qualified solution is found in the previous cases. The derivation of the solution is provided in the Appendix.

The pseudocode in Fig. 8 summarizes the procedure for reconstructing the image from the decomposed sinograms. We initialize the image and the error sinogram with the raw FBP images. Then within each iteration, for each selected voxel j, we first compute the jth column of the forward projection matrix, which is $A_{*,j}$, by using the distance driven method [45]. Second, we compute the first two derivatives of the log-likelihood function, θ_1 and θ_2. Third, we compute the surrogate prior coefficients, ψ_r, for each of the neighboring voxels by using (43) and (45). Fourth, we compute the first two derivatives for the quadratic cost function, ϕ_1 and ϕ_2, by using (46) and (47). Fifth, we solve the optimization problem in (48) by using the KKT condition to obtain the voxel update. Finally, we update the error sinogram by forward projecting the voxel update and update the image as well.

IV. Experimental Results

We have applied the proposed JDE-MBIR algorithm to real 3-D DECT reconstruction problems. Raw data were acquired on a Discovery CT750 HD scanner (GE Healthcare, WI, USA) in a dual-energy fast switching acquisition mode, with the X-ray tube voltage alternating between 80 and 140 kVp from view to view. This spectral CT imaging technique is also referred to as gemstone spectral imaging (GSI). Each scan contains approximately 2500 views per rotation, with each kVp having the same

number of views, which is approximately 1250. Each scan was made with a large bowtie present. Each of the reconstructed images has a thickness of 0.625 mm, with 512 × 512 pixels. We reconstruct with water and iodine sinograms after material decomposition, with each material having the same number of views per rotation, which is approximately 2500. The reconstructed images represent the cross sections corresponding to water- and iodine-equivalent densities in units of mg/cm^3. The "monochromatic" image, which specifies the cross section corresponding to the attenuation given the photon energy, can then be generated by a linear combination of the reconstructed density images as in (18). Note that we do not generate monochromatic sinograms for reconstruction.

The function h^{-1} in (25) is approximated by using a high order polynomial with the following form:

$$\begin{aligned}&[\hat{p}_{i,\mathrm{W}}, \hat{p}_{i,\mathrm{I}}]\\ &\quad = h^{-1}(y_{i,\mathrm{l}}, y_{i,\mathrm{h}})\\ &\quad = \left[\sum_{m=0}^{L}\sum_{n=0}^{L} c_{m,n,\mathrm{W}} y_{i,\mathrm{l}}^m y_{i,\mathrm{h}}^n, \sum_{m=0}^{L}\sum_{n=0}^{L} c_{m,n,\mathrm{I}} y_{i,\mathrm{l}}^m y_{i,\mathrm{h}}^n\right] \quad (49)\end{aligned}$$

with $L = 10$. The specific coefficients for the polynomial, denoted by $\{c_{m,n,\mathrm{W}}, c_{m,n,\mathrm{I}}\}$, $\forall m \in \{0, 1, \cdots, L\}$, $\forall n \in \{0, 1, \cdots, L\}$, are computed in a calibration procedure for each device, as described in [57]. As described in Section II-B, these coefficients depend on many specific details of the device's physics including the X-ray spectra and detector sensitivity. The coefficients of the material decomposition are estimated in two stages. First, a polynomial is estimated to correct for beam hardening on a water phantom, and then the full set of coefficients are estimated for complete material decomposition.

We will compare the proposed JDE-MBIR method with two other decomposition-based methods, one using FBP reconstruction and the other using independent DE-MBIR. The FBP method consists of first obtaining two material sinograms from the material decomposition and then performing FBP on each sinogram with a standard reconstruction filter kernel. Then the resulting material density images are processed by a correlation-based noise reduction method [40], [58]. The independent DE-MBIR was implemented in the same way as described in Section II-D. That is, the off-diagonal terms of the weighting matrix, B_i, were set to 0. All of the above methods work with the same decomposed sinograms. In practice, we implement the interleaved nonhomogeneous ICD algorithm [24] for both independent DE-MBIR and JDE-MBIR. This method focuses computation where updates are mostly needed, which consequently accelerates the convergence. Both the independent DE-MBIR and JDE-MBIR are implemented on a standard 2.53-GHz clock rate 8 core Intel processor workstation with the Linux operating system. For both methods, we run 10 iterations to obtain the fully converged results.

In order to compare fairly among different reconstruction methods, for each experiment we match the noise level in 70 keV monochromatic images. That is, the difference of the noise standard deviation measured within a fixed ROI is less than 1 HU among different methods. We adjust the prior strength, $b_{jk,s}$ in (31), to match the noise level.

We first evaluate the performance of different methods using the phantom. For quantitative assessment, we use a 20-cm-diameter GE Performance Phantom (GEPP) scanned in 64 × 0.625 mm helical mode at pitch 0.938:1 in 540 mAs in 300 mm field-of-view (FOV). The GEPP contains a Plexiglas insert with resolution bars and a 50-μm-diameter tungsten wire placed in water. We measure the standard deviation within a fixed ROI in a homogeneous region of Plexiglas for noise assessment, and also measure the modulation transfer function (MTF) by using the wire for in-plane resolution assessment [59]. The width of the MTF is proportional to the spatial resolution. In this paper, 10% MTF is chosen for comparison, since it generally reflects the visual resolution of the image. In addition to the above wire method, we also use the cyclic bar patterns to measure the spatial resolution. Following the method described in [60], we compute the MTF gain as the image modulation divided by the object modulation.

The JDE-MBIR method improves the spatial resolution and simultaneously reduces noise in the phantom study. This is illustrated by the GEPP reconstructions shown in Fig. 9. As shown in the figure, JDE-MBIR provides greater noise suppression than FBP and independent DE-MBIR in both water and iodine images, which leads to visually smoother homogeneous regions. Meanwhile, JDE-MBIR improves the resolution by producing a less blurred wire spot and spatially more distinguishable bars. One can also observe the resolution improvement in the monochromatic images in Fig. 10, which are synthesized using the reconstructed material densities in Fig. 9 following (18). The increased visual separation of the bars is illustrated by the profile plots in Fig. 11.

The visual improvement on the GEPP reconstruction is further verified by quantitative measurements in Table I. With comparable noise level in 70 keV monochromatic images, JDE-MBIR significantly reduces noise as compared to FBP and independent DE-MBIR, especially for water images. JDE-MBIR also improves the in-plane resolution substantially as compared to FBP and independent DE-MBIR, according to these two different resolution metrics.

Figs. 13 and 14 show the resolution and noise of the monochromatic images across various photon energies, where we match the noise level at 70 keV for different methods for comparison. Fig. 12 presents the monochromatic images at two distinct energies as an example. As shown in Fig. 13, JDE-MBIR significantly raises the resolution as compared to FBP and independent DE-MBIR. Fig. 14 also shows this resolution improvement by investigating the bar patterns at three different spatial frequencies. Each plot is computed using the method described in [60]. Note that for each frequency, the JDE-MBIR produces the largest contrast (i.e., closest to an ideal value of 100%) across all energies. This is consistent with the visual quality of the resolution bars in Figs. 10 and 12.

In addition, Fig. 13 shows that the JDE-MBIR monochromatic image contains less noise than the FBP image for all energies of diagnostic interest. It also has a more tractable noise characteristic than the monochromatic image with the independent DE-MBIR. More precisely, although the independent

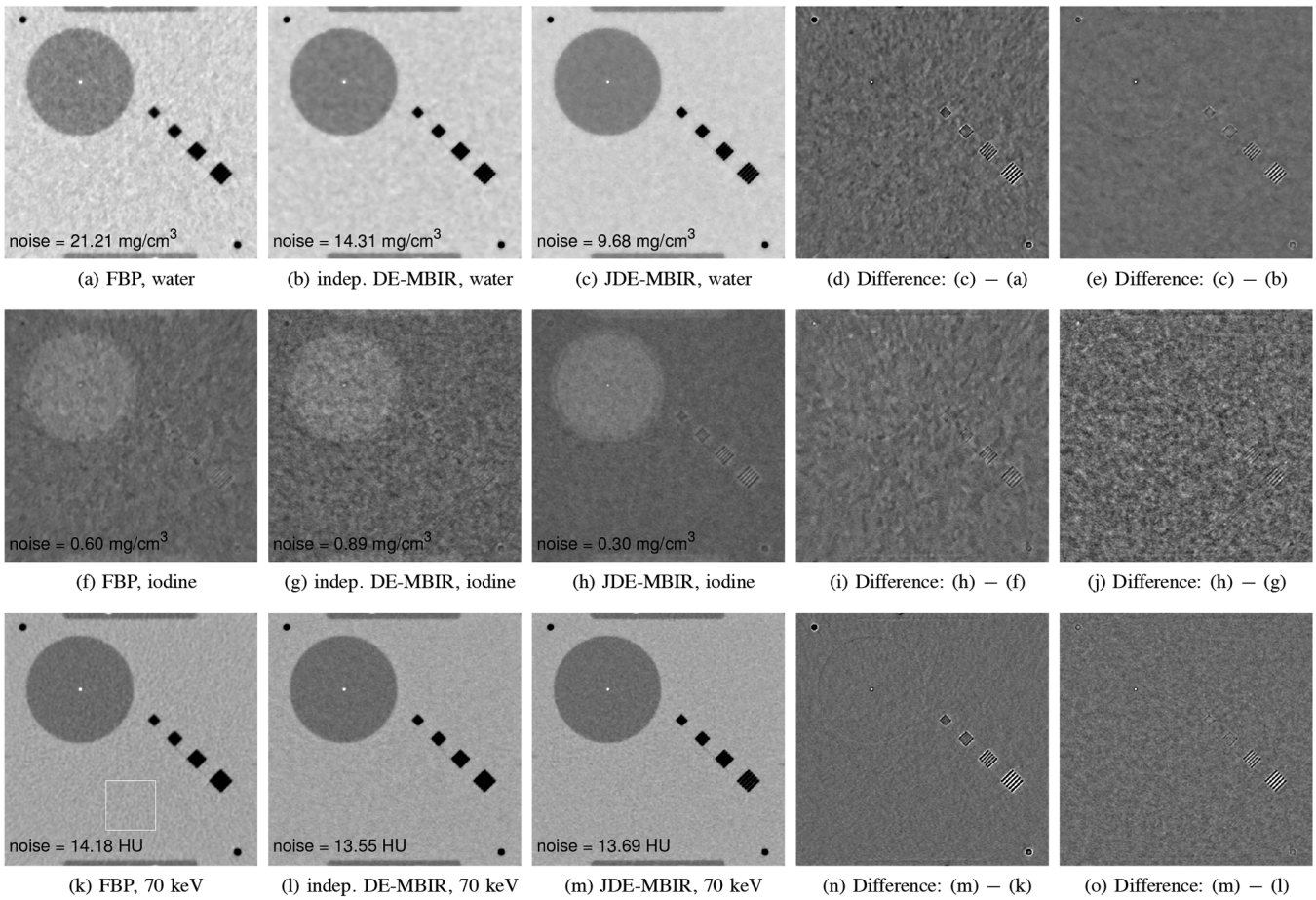

(a) FBP, water (b) indep. DE-MBIR, water (c) JDE-MBIR, water (d) Difference: (c) − (a) (e) Difference: (c) − (b)

(f) FBP, iodine (g) indep. DE-MBIR, iodine (h) JDE-MBIR, iodine (i) Difference: (h) − (f) (j) Difference: (h) − (g)

(k) FBP, 70 keV (l) indep. DE-MBIR, 70 keV (m) JDE-MBIR, 70 keV (n) Difference: (m) − (k) (o) Difference: (m) − (l)

Fig. 9. Comparison of FBP, independent DE-MBIR (indep. DE-MBIR) and JDE-MBIR reconstructions from a GEPP scan. From top to bottom: water density image, iodine density, and 70 keV monochromatic image. From left to right: FBP, independent DE-MBIR, JDE-MBIR, difference between JDE-MBIR and FBP, difference between JDE-MBIR and independent DE-MBIR. Display window for water images: window width (WW) 600 mg/cm^3 and window level (WL) 950 mg/cm^3; for water difference images: WW 600 mg/cm^3 and WL 0 mg/cm^3; for iodine images: WW 15 mg/cm^3 and WL -0.5 mg/cm^3; for iodine difference images: WW 7.5 mg/cm^3 and WL 0 mg/cm^3; for monochromatic images: WW 600 HU and WL 0 HU; for mono difference images: WW 300 HU and WL 0 HU. The white box on the 70 keV FBP image (first at the third row) indicates the region where the noise standard deviation is evaluated.

(a) FBP (b) indep. DE-MBIR (c) JDE-MBIR

Fig. 10. Resolution bars in the 70 keV monochromatic images from a GEPP scan reconstructed with: (a) FBP; (b) independent DE-MBIR; (c) JDE-MBIR. Display window: WW 200 HU and WL -400 HU. Each image zooms in to the resolution bars of the monochromatic images shown in Fig. 9 with a different display window.

DE-MBIR monochromatic image appears slightly less noisy than the JDE-MBIR monochromatic image for some energy levels, the noise rises rapidly for the independent model as energy decreases. This is because the iodine component dominates the photon attenuation at low energy and the independent DE-MBIR method tends to produce noisy iodine reconstructions. Also, optimizing the prior strength for independent DE-MBIR becomes difficult due to this huge variation. This result also indicates that one can further reduce noise while still earning the advantage in spatial resolution by using the JDE-MBIR.

We also compared the convergence speed of the JDE-MBIR and the standard single-energy MBIR [24] with the GEPP reconstruction to measure the additional computational burden occasioned by the dual-energy reconstruction. For single-energy MBIR, we simply took the water sinogram and weight from the data used in the experiment of Fig. 9 and performed the reconstruction. In this case, the data used in JDE-MBIR and single-energy MBIR share the same scanner geometry and settings such as helical pitch, rotation speed, and local statistics for the water component. Note that the resulting single-energy MBIR reconstruction has no particularly quantitative meaning, but it is still useful for comparing the computation time. Both algorithms were implemented on the same software platform and run on the same hardware. Fig. 15 shows the comparison of convergence speed between JDE-MBIR and single-energy MBIR. Since these two methods do not reach the same final cost due to different cost functions, we scale the cost of the single-energy MBIR such that it has the same final cost as JDE-MBIR, assuming full convergence has been reached in 10 iterations as

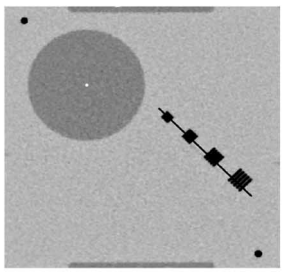

(a) profile line on the image

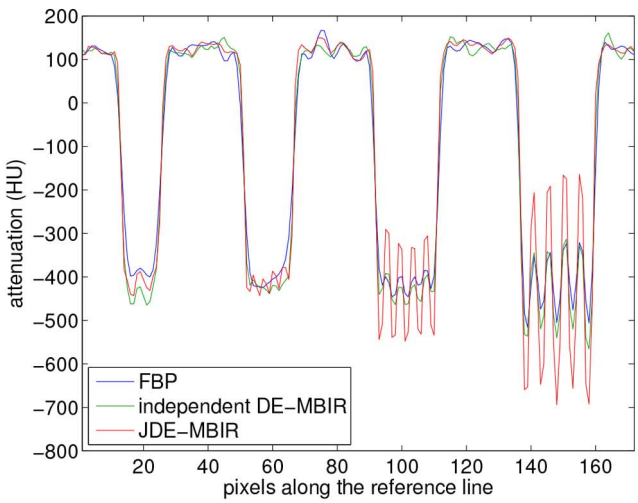

(b) attenuations along the profile line

Fig. 11. Profile plot across the resolution bars on the GEPP 70 keV monochromatic images for FBP, independent DE-MBIR, and JDE-MBIR. Top: profile line on the image; bottom: attenuations along the profile line with FBP (blue), independent DE-MBIR (green), and JDE-MBIR (red).

TABLE I
COMPARISON OF FBP, INDEPENDENT DE-MBIR, AND JDE-MBIR FOR MEASUREMENT OF NOISE AND IN-PLANE RESOLUTION FOR THE IMAGES IN FIG. 9. RESOLUTION MEASURED BY USING THE CYCLIC BARS METHOD IS MADE IN THE 70 keV MONOCHROMATIC IMAGES AT THE THREE LOWEST SPATIAL FREQUENCIES

Noise Measurement (Standard Deviation)			
	water (mg/cm^3)	iodine (mg/cm^3)	70 keV mono. (HU)
FBP	21.21	0.60	14.18
Independent DE-MBIR	14.31	0.89	13.55
JDE-MBIR	9.68	0.30	13.69

Resolution Measurement (10% MTF by the wire method)			
	water (lp/cm)	iodine (lp/cm)	70 keV mono. (lp/cm)
FBP	6.15	5.81	6.60
Independent DE-MBIR	8.61	6.35	8.90
JDE-MBIR	11.80	10.59	11.70

Resolution Measurement (MTF gain by the cyclic bars method)			
	6.25 lp/cm (%)	7.69 lp/cm (%)	10 lp/cm (%)
FBP	11.55	3.70	0
Independent DE-MBIR	15.35	3.74	0.25
JDE-MBIR	40.30	19.10	3.28

usually observed in practice. As shown in the figure, both algorithms converge within four iterations. In this experiment, the average total computation time per iteration for JDE-MBIR was 1.47 times the computation required for single-energy MBIR as measured across about 9 million voxels located differently in the 3-D FOV. The main reason for the increase in computation stems from the fact that the sinograms for JDE-MBIR contain twice as much data as that for single-energy MBIR because of interpolation.

We also evaluated the reconstruction accuracy of JDE-MBIR by using a GE GSI contrast phantom, which was scanned in 32 $\times$ 0.625 mm axial mode in 384 mAs in 500 mm FOV. This phantom consists of a water phantom with several cylindrical rods inserted, each containing known concentrations of iodine and water. Fig. 16 shows the JDE-MBIR reconstructions of this phantom, with the theoretical iodine and water densities given in Table II. Fig. 16 also plots the reconstructed iodine and water densities for FBP and JDE-MBIR. For each rod with known iodine concentration, we calculated the average of the reconstructed values in an ROI within the rod. As shown in the plots, FBP and JDE-MBIR produce equally accurate material densities.

We also compared FBP, independent DE-MBIR, and JDE-MBIR by using real clinical data, as shown in Figs. 17 and 18. The data were collected from an abdominal scan in 64 $\times$ 0.625 mm helical mode at pitch 0.984:1 in 540 mAs in 500 mm FOV. Fig. 17 shows that the JDE-MBIR dramatically reduces the noise in the homogeneous regions (e.g., liver) in both water and iodine images. The bone structures in the JDE-MBIR water image also suffer from less blooming and have sharper edges than the other two methods. Meanwhile, the JDE-MBIR improves the resolution in the iodine image as compared to the other two methods. For example, one can see details such as liver vessels more clearly in the JDE-MBIR image.

Fig. 18 presents the corresponding monochromatic images at various energies. The resolution improvement can be observed in the JDE-MBIR images as compared to the other two methods, with a fixed noise level in the 70 keV monochromatic image. However, according to the resolution and noise curves shown in Fig. 13, one can achieve less noise while still retaining better resolution for the JDE-MBIR method as compared to the FBP method, by adjusting the prior strength. These results illustrate the potential diagnostic benefits of the JDE-MBIR method for DECT reconstruction. Note that either JDE-MBIR or independent DE-MBIR can be further improved by tuning the parameters for a particular clinical application.

V. CONCLUSION

In this paper, we have presented a JDE-MBIR approach for DECT reconstruction. The proposed method combines a joint likelihood model to account for the noise correlation in material-decomposed sinograms with MRF regularization, and features a physically realistic constraint that ensures nonnegative X-ray absorptions. We also demonstrate that the JDE-MBIR method retains a more accurate model of the data likelihood than other decomposition-based statistical iterative methods when DECT uses fast kVp switching techniques. The experimental results on phantom and clinical data show that the JDE-MBIR

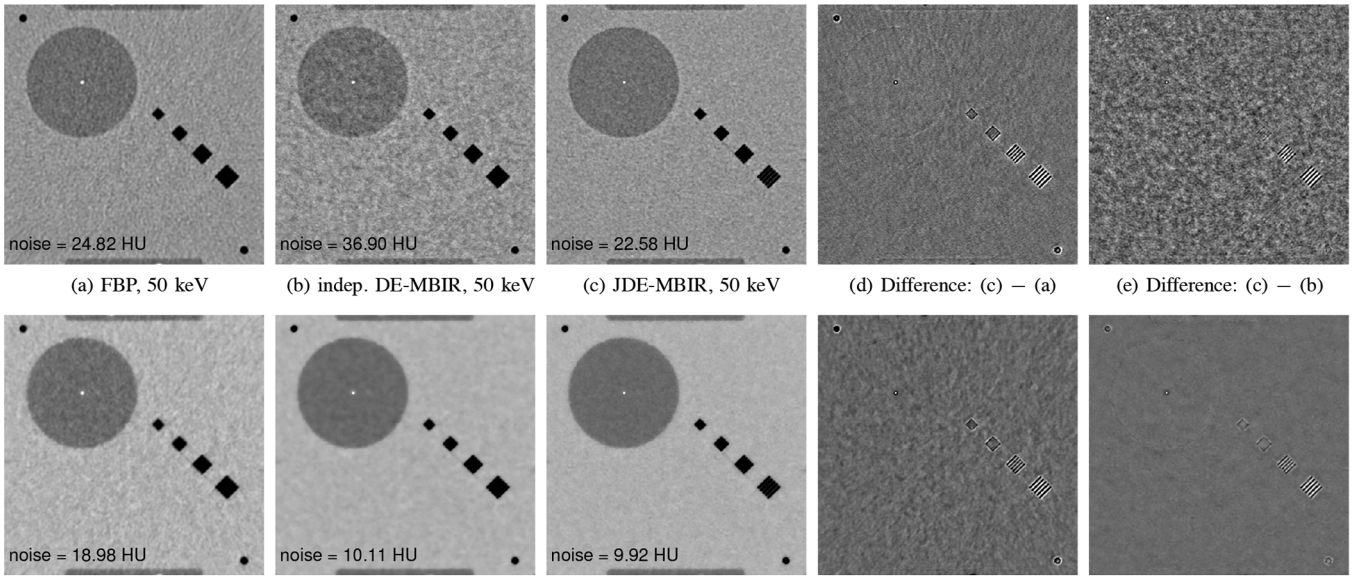

(a) FBP, 50 keV (b) indep. DE-MBIR, 50 keV (c) JDE-MBIR, 50 keV (d) Difference: (c) − (a) (e) Difference: (c) − (b)

(f) FBP, 130 keV (g) indep. DE-MBIR, 130 keV (h) JDE-MBIR, 130 keV (i) Difference: (h) − (f) (j) Difference: (h) − (g)

Fig. 12. Comparison of FBP, independent DE-MBIR (indep. DE-MBIR), and JDE-MBIR monochromatic images of the GEPP at different energies. From top to bottom: photon energy at 50 and 130 keV. From left to right: FBP, independent DE-MBIR, JDE-MBIR, difference between JDE-MBIR and FBP, difference between JDE-MBIR and independent DE-MBIR. Display window for monochromatic images: WW 600 HU and WL 0 HU; for difference images: WW 300 HU and WL 0 HU. These monochromatic images are synthesized using the reconstructed material densities shown in Fig. 9 based on (18).

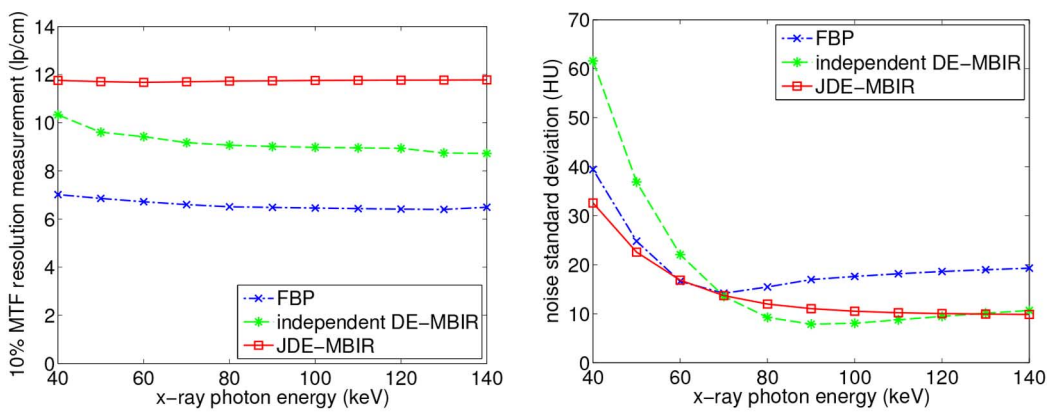

(a) in-plane resolution (b) noise standard deviation

Fig. 13. Resolution and noise of the monochromatic images across various energy levels with different reconstruction methods.

method can reduce noise and increase resolution as compared to the FBP method and the independent DE-MBIR method. We expect that the improvement in terms of lower noise and higher resolution brought by the JDE-MBIR method may potentially reduce the CT dose required for a particular image quality. Future investigation will assess how to further improve material separation performance and investigate potential clinical benefits.

APPENDIX
DERIVATION OF THE SOLUTION

We derive the solution to the 2-D quadratic minimization problem defined in (48). The optimization problem is given by

$$\begin{aligned} \min_{u} \quad & \frac{1}{2} u \phi_2 u^T + u \phi_1 + const. \\ \text{s.t.} \quad & u \cdot n_{\min} \geq 0 \quad \text{and} \quad u \cdot n_{\max} \geq 0 \end{aligned}$$

where $u \in \Re^2$ and

$$\begin{aligned} \phi_1 &= [\phi_1(1), \phi_1(2)]^T \\ \phi_2 &= \begin{bmatrix} \phi_2(1,1) & \phi_2(1,2) \\ \phi_2(1,2) & \phi_2(2,2) \end{bmatrix} \\ n_{\min} &= [n_{\min}(1), n_{\min}(2)] \\ n_{\max} &= [n_{\max}(1), n_{\max}(2)] . \end{aligned}$$

We solve this problem by using the KKT condition. The KKT condition states that a valid solution u should satisfy

$$\begin{cases} \phi_2 u^T + \phi_1 - \lambda_1 n_{\min}^T - \lambda_2 n_{\max}^T = 0 \\ \lambda_1 \cdot u \cdot n_{\min} = 0 \\ \lambda_2 \cdot u \cdot n_{\max} = 0 \\ u \cdot n_{\min} \geq 0 \\ u \cdot n_{\max} \geq 0 \\ \lambda_1, \lambda_2 \geq 0 \end{cases} \tag{50}$$

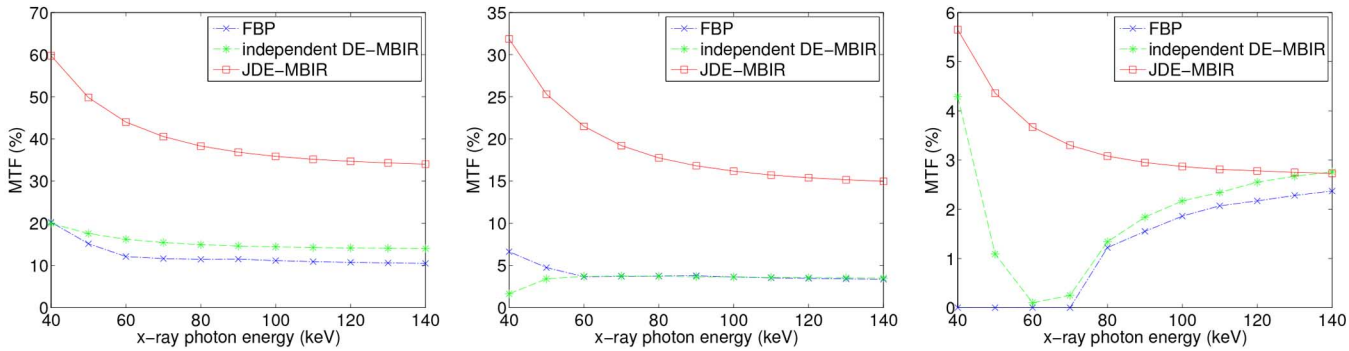

(a) cyclic bars with frequency of 6.25 lp/cm (b) cyclic bars with frequency of 7.69 lp/cm (c) cyclic bars with frequency of 10 lp/cm

Fig. 14. MTF measured at the cyclic bars of three different spatial frequencies in the monochromatic images across various photon energies. JDE-MBIR produces higher MTF values than the other two methods at all three frequencies.

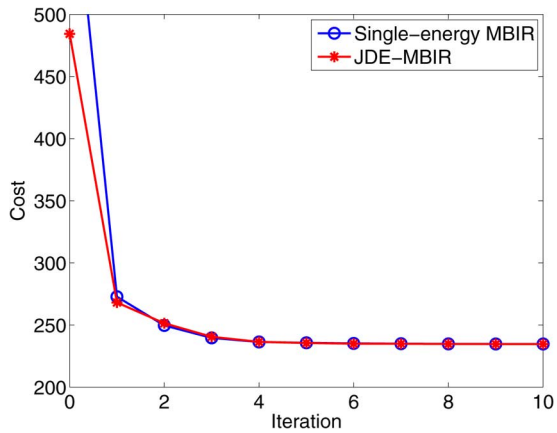

Fig. 15. Comparison of the convergence speed of the JDE-MBIR and the standard single-energy MBIR with the GEPP reconstruction in Fig. 9. The cost for the single-energy MBIR is scaled such that it reaches the same final cost as JDE-MBIR.

TABLE II
THEORETICAL DENSITIES OF IODINE AND WATER FOR THE INSERTED RODS IN THE GSI CONTRAST PHANTOM AS SHOWN IN FIG. 16

Rod	1	2	3	4	5	6
Iodine (mg/cm^3)	0	2.5	5	7.5	15	20
Water (mg/cm^3)	1000	999.5	999	998.5	997	995.9

where λ_1 and λ_2 are the KKT multipliers. Then we can compute the solution within four different cases, i.e., ($\lambda_1 = 0$, $\lambda_2 = 0$), ($\lambda_1 > 0$, $\lambda_2 = 0$), ($\lambda_1 = 0$, $\lambda_2 > 0$), and ($\lambda_1 > 0$, $\lambda_2 > 0$). Within each case, we compute the solution by using the equality conditions and then test the resulting solution with the inequality conditions. Since the cost function and the constraints in this problem are all continuously differentiable and convex, the KKT condition is both necessary and sufficient [56]. Thus, a solution becomes our updated value if and only if it satisfies both the equality and inequality conditions.

1) $\lambda_1 = 0, \lambda_2 = 0$. This combination gives the unconstrained solution, which can be computed from the first equation in (50) as

$$u = -\phi_2^{-1}\phi_1. \tag{51}$$

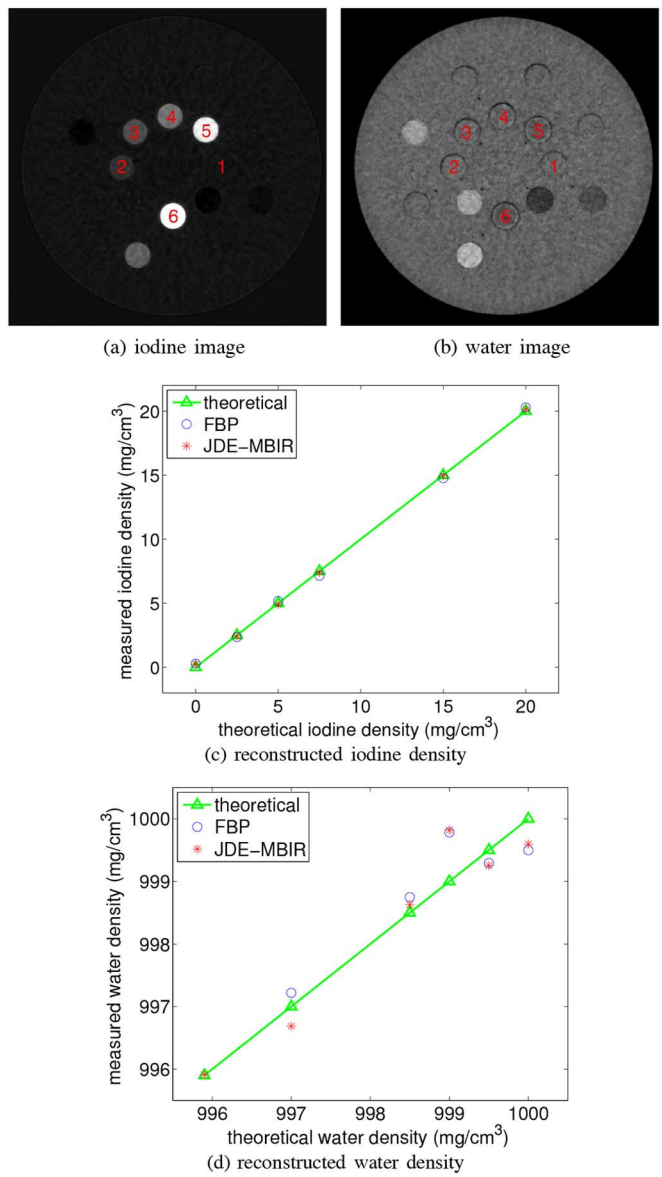

(a) iodine image (b) water image
(c) reconstructed iodine density
(d) reconstructed water density

Fig. 16. Top row shows the JDE-MBIR reconstructions of the GE GSI contrast phantom. This phantom consists of a water phantom base and several cylindrical rods, each of which contains certain concentrations of iodine and water. Display window for water image: WW 600 mg/cm^3, WL 1000 mg/cm^3; for iodine image: WW 17.5 mg/cm^3, WL 7.5 mg/cm^3. Bottom two rows show the reconstruction accuracy of FBP and JDE-MBIR for iodine and water.

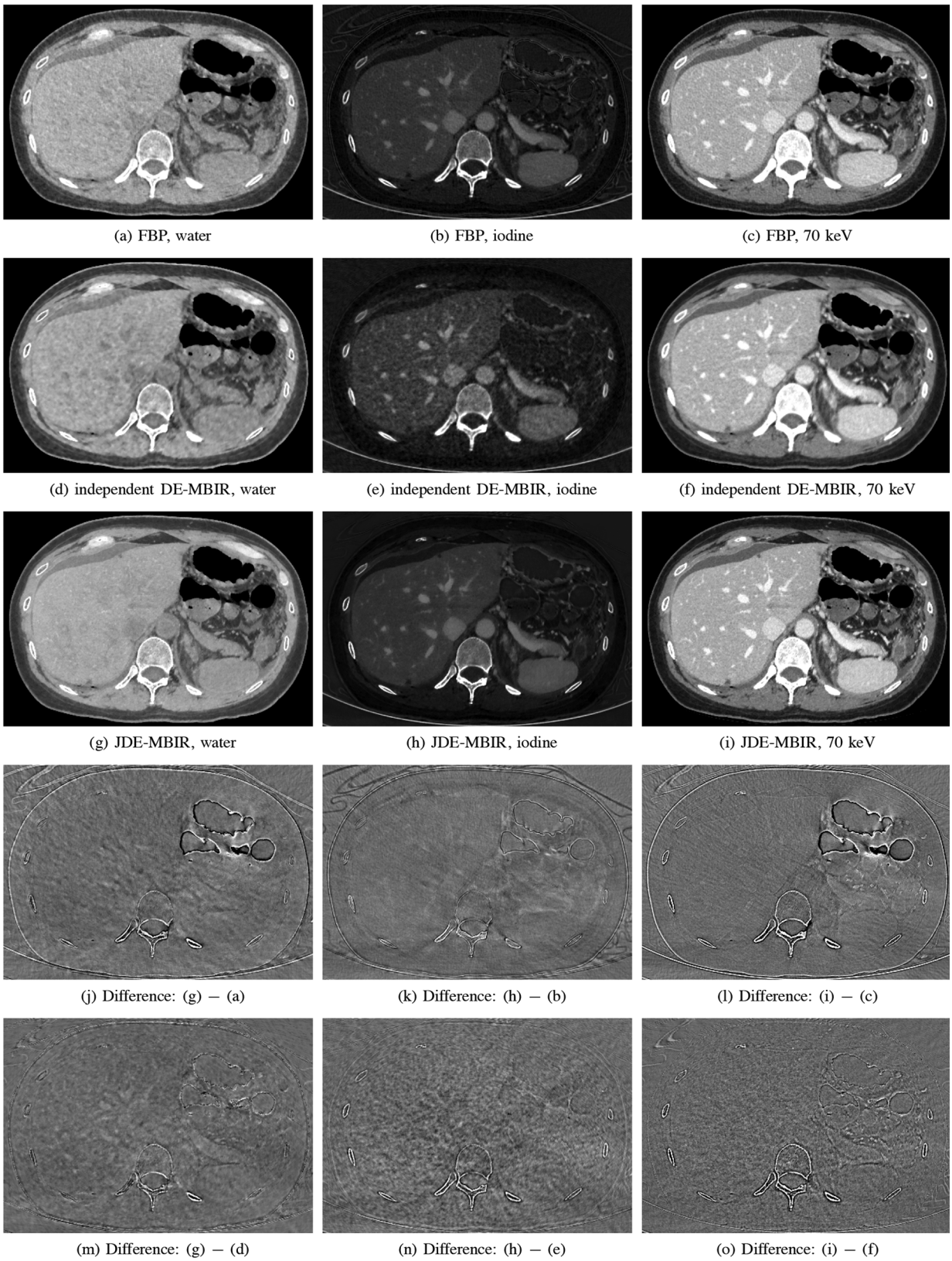

Fig. 17. Comparison of FBP, independent DE-MBIR and JDE-MBIR reconstructions for an abdominal clinical scan. From top to bottom: FBP, independent DE-MBIR, JDE-MBIR, difference between JDE-MBIR and FBP, difference between JDE-MBIR and independent DE-MBIR. From left to right: water density image, iodine density image, and 70 keV monochromatic image. Display window for water images: WW 300 mg/cm^3 and WL 1000 mg/cm^3; for water difference images: WW 200 mg/cm^3 and WL 0 mg/cm^3; for iodine images: WW 17.5 mg/cm^3 and WL 6.5 mg/cm^3; for iodine difference images: WW 9 mg/cm^3 and WL 0 mg/cm^3; for monochromatic images: WW 400 HU and WL 40 HU; for mono difference images: WW 200 HU and WL 0 HU.

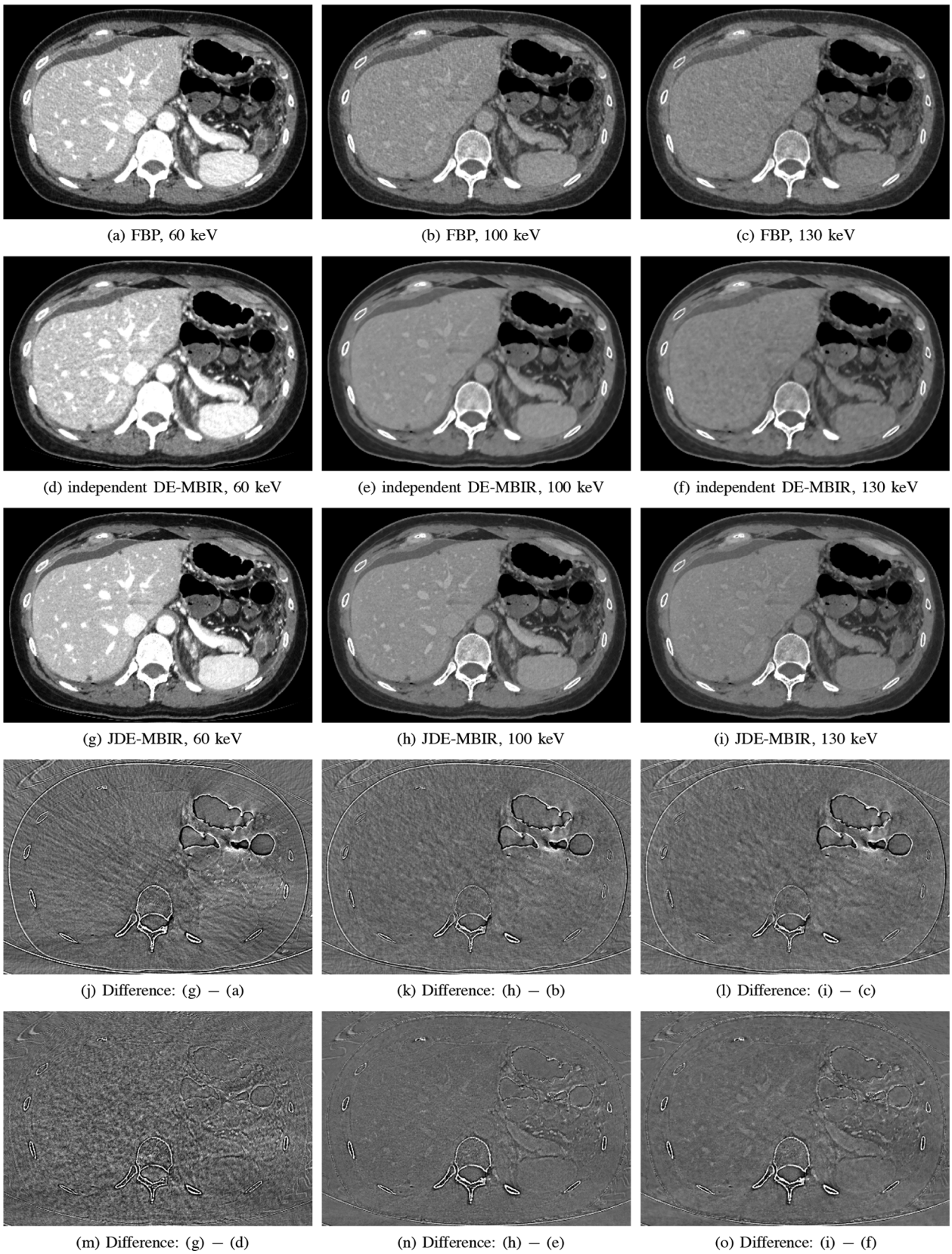

(a) FBP, 60 keV (b) FBP, 100 keV (c) FBP, 130 keV

(d) independent DE-MBIR, 60 keV (e) independent DE-MBIR, 100 keV (f) independent DE-MBIR, 130 keV

(g) JDE-MBIR, 60 keV (h) JDE-MBIR, 100 keV (i) JDE-MBIR, 130 keV

(j) Difference: (g) − (a) (k) Difference: (h) − (b) (l) Difference: (i) − (c)

(m) Difference: (g) − (d) (n) Difference: (h) − (e) (o) Difference: (i) − (f)

Fig. 18. Comparison of FBP, independent DE-MBIR and JDE-MBIR performance on monochromatic images of an abdominal clinical scan at various energies. From top to bottom: FBP, independent DE-MBIR, JDE-MBIR, difference between JDE-MBIR and FBP, difference between JDE-MBIR and independent DE-MBIR. From left to right: photon energy at 60, 100, and 140 keV. Display window: WW 400 HU and WL 40 HU; for mono difference images: WW 200 HU and WL 0 HU. These monochromatic images are synthesized using the reconstructed material densities shown in Fig. 17 based on (18).

Then, we need to test this solution with the following inequality conditions:

$$\begin{cases} u \cdot n_{\min} \geq 0 \\ u \cdot n_{\max} \geq 0 \end{cases}. \tag{52}$$

2) $\lambda_1 > 0$, $\lambda_2 = 0$. In this case, we solve the optimization problem on the boundary with $u \cdot n_{\min} = 0$. This combination leads to the following:

$$\begin{bmatrix} \phi_2 & -n_{\min}^T \\ -n_{\min} & 0 \end{bmatrix} \begin{bmatrix} u^T \\ \lambda_1 \end{bmatrix} = \begin{bmatrix} -\phi_1 \\ 0 \end{bmatrix}. \tag{53}$$

The solution is given by

$$\begin{cases} u^T = -\left(\phi_2^{-1} - \dfrac{\phi_2^{-1} n_{\min}^T n_{\min} \phi_2^{-1}}{n_{\min} \phi_2^{-1} n_{\min}^T}\right) \phi_1 \\ \lambda_1 = \dfrac{n_{\min}^T \phi_2^{-1} \phi_1}{n_{\min} \phi_2^{-1} n_{\min}^T} \end{cases}. \tag{54}$$

This solution needs to be tested with

$$\begin{cases} u \cdot n_{\max} \geq 0 \\ \lambda_1 > 0 \end{cases}. \tag{55}$$

3) $\lambda_1 = 0$, $\lambda_2 > 0$. In this case, we solve the optimization problem on the boundary with $u \cdot n_{\max} = 0$. Similarly to the previous case, this combination gives the solution

$$\begin{cases} u^T = -\left(\phi_2^{-1} - \dfrac{\phi_2^{-1} n_{\max}^T n_{\max} \phi_2^{-1}}{n_{\max} \phi_2^{-1} n_{\max}^T}\right) \phi_1 \\ \lambda_2 = \dfrac{n_{\max}^T \phi_2^{-1} \phi_1}{n_{\max} \phi_2^{-1} n_{\max}^T} \end{cases}. \tag{56}$$

This solution needs to be tested with

$$\begin{cases} u \cdot n_{\min} \geq 0 \\ \lambda_2 > 0 \end{cases}. \tag{57}$$

4) $\lambda_1 > 0$, $\lambda_2 > 0$. With this combination, the only feasible solution is $u = [0, 0]$.

In practice, we test the four cases sequentially. Once all the equality and inequality conditions are satisfied, the solution becomes the desired voxel update. This process is shown in Fig. 7.

ACKNOWLEDGMENT

The authors would like to thank anonymous reviewers for their valuable comments.

REFERENCES

[1] W. A. Kalender, W. H. Perman, J. R. Vetter, and E. Klotz, "Evaluation of a prototype dual-energy computed tomographic apparatus. I. Phantom studies," *Med. Phys.*, vol. 13, no. 3, pp. 334–339, May/Jun. 1986.

[2] T. Johnson, B. Krau, M. Sedlmair, M. Grasruck, H. Bruder, D. Morhard, C. Fink, S. Weckbach, M. Lenhard, B. Schmidt, T. Flohr, M. F. Reiser, and C. R. Becker, "Material differentiation by dual energy CT: Initial experience," *Eur. J. Radiol.*, vol. 17, no. 6, pp. 1510–1517, Jun. 2007.

[3] S. Singh and M. Singh, "Explosives detection systems (EDS) for aviation security," *Signal Process.*, vol. 83, no. 1, pp. 31–55, Jan. 2003.

[4] Z. Ying, R. Naidu, and C. R. Crawford, "Dual energy computed tomography for explosive detection," *J. X-Ray Sci. Tech.*, vol. 14, pp. 235–256, 2006.

[5] P. Engler and W. Friedman, "Review of dual-energy computed tomography techniques," *Mater. Eval.*, vol. 48, pp. 623–629, 1990.

[6] R. E. Alvarez and A. Macovski, "Energy-selective reconstructions in X-ray computerized tomography," *Med. Phys.*, vol. 21, no. 5, pp. 733–744, Sep. 1976.

[7] L. A. Lehmann, R. E. Alvarez, A. Macovski, W. R. Brody, N. J. Pelc, S. J. Riederer, and A. L. Hall, "Generalized image combinations in dual KVP digital radiography," *Med. Phys.*, vol. 8, no. 5, pp. 659–667, Sep./Oct. 1981.

[8] W. R. Brody, G. Butt, A. Hall, and A. Macovski, "A method for selective tissue and bone visualization using dual energy scanned projection radiography," *Med. Phys.*, vol. 8, no. 3, pp. 353–357, May/Jun. 1981.

[9] K.-S. Chuang and H. K. Huang, "A fast deal-energy computational method using isotransmission lines and table lookup," *Med. Phys.*, vol. 14, no. 2, pp. 186–192, Mar./Apr. 1987.

[10] H. N. Cardinal and A. Fenster, "An accurate method for direct dual-energy calibration and decomposition," *Med. Phys.*, vol. 17, no. 3, pp. 327–341, May/Jun. 1990.

[11] B. Brendel, E. Roessl, J.-P. Schlomka, and R. Proksa, "Empirical, projection-based basis-component decomposition method," in *Proc. SPIE Med. Imag.: Phys. Med. Imag.*, 2009, p. 72583Y.

[12] P. Stenner, T. Berkus, and M. Kachelrieß, "Empirical dual energy calibration (EDEC) for cone-beam computed tomography," *Med. Phys.*, vol. 34, no. 9, pp. 3630–3641, Sep. 2007.

[13] U. Hassler, L. Garnero, and P. Rizo, "X-ray dual-energy calibration based on estimated spectral properties of the experimental system," *IEEE Trans. Nucl. Sci.*, vol. 45, pp. 1699–1712, Jun. 1998.

[14] Y. Zou and M. D. Silver, "Analysis of fast kV-switching in dual energy CT using a pre-reconstruction decomposition technique," in *Proc. SPIE Med. Imag,: Phys. Med. Imag.*, 2008, p. 691313.

[15] J. Noh, J. A. Fessler, and P. E. Kinahan, "Statistical sinogram restoration in dual-energy CT for PET attenuation correction," *IEEE Trans. Med. Imag.*, vol. 28, no. 11, pp. 1688–1702, Nov. 2009.

[16] R. A. Brooks, "A quantitative theory of the Hounsfield unit and its application to dual energy scanning," *J. Comput. Assist. Tomogr.*, vol. 1, no. 4, pp. 487–493, 1977.

[17] P. Joseph and R. Spital, "A method for correcting bone induced artifacts in computed tomography scanners," *J. Comput. Assist. Tomogr.*, vol. 2, no. 1, pp. 100–108, 1978.

[18] B. J. Heismann, J. Leppert, and K. Stierstorfer, "Density and atomic number measurements with spectral x-ray attenuation method," *J. Appl. Phys.*, vol. 94, no. 3, pp. 2073–2079, 2003.

[19] C. Maaß, M. Baer, and M. Kachelrieß, "Image-based dual energy CT using optimized precorrection functions: A practical new approach of material decomposition in image domain," *Med. Phys.*, vol. 36, no. 8, pp. 3818–3829, 2009.

[20] C. Maaß, E. Meyer, and M. Kachelrieß, "Exact dual energy material decomposition from inconsistent rays (MDIR)," *Med. Phys.*, vol. 38, no. 2, pp. 691–700, 2011.

[21] J.-B. Thibault, K. D. Sauer, J. Hsieh, and C. A. Bouman, "A three-dimensional statistical approach to improve image quality for multislice helical CT," *Med. Phys.*, vol. 34, no. 11, pp. 4526–4544, Nov. 2007.

[22] G. Wang, H. Yu, and B. De Man, "An outlook on X-ray CT research and development," *Med. Phys.*, vol. 35, no. 3, pp. 1051–1064, 2008.

[23] A. Ziegler, T. Kohler, and R. Proksa, "Noise and resolution in images reconstructed with FBP and OSC algorithms for CT," *Med. Phys.*, vol. 34, no. 2, pp. 585–598, 2007.

[24] Z. Yu, J.-B. Thibault, C. A. Bouman, K. D. Sauer, and J. Hsieh, "Fast model-based X-ray CT reconstruction using spatially nonhomogeneous ICD optimization," *IEEE Trans. Image Process.*, vol. 20, no. 1, pp. 161–175, Jan. 2011.

[25] K. D. Sauer and C. A. Bouman, "A local update strategy for iterative reconstruction from projections," *IEEE Trans. Signal Process.*, vol. 41, no. 2, pp. 534–548, Feb. 1993.

[26] C. A. Bouman and K. D. Sauer, "A unified approach to statistical tomography using coordinate descent optimization," *IEEE Trans. Image Process.*, vol. 5, no. 3, pp. 480–492, Mar. 1996.

[27] R. C. Nelson, S. Feuerlein, and D. T. Boll, "New iterative reconstruction techniques for cardiovascular computed tomography: How do they work, and what are the advantages and disadvantages?," *J. Cardiovasc. Comput. Tomogr.*, vol. 5, no. 5, pp. 286–292, 2011.

[28] H. Scheffel, P. Stolzmann, C. L. Schlett, L.-C. Engel, G. P. Major, M. Károlyi, S. Do, P. Maurovich-Horvat, and U. Hoffmann, "Coronary artery plaques: Cardiac CT with model-based and adaptive-statistical iterative reconstruction technique," *Eur. J. Radiol.*, vol. 81, no. 3, pp. e363–e369, 2012.

[29] D. B. Husarik, D. Marin, E. Samei, S. Richard, B. Chen, T. A. Jaffe, M. R. Bashir, and R. C. Nelson, "Radiation dose reduction in abdominal computed tomography during the late hepatic arterial phase using a model-based iterative reconstruction algorithm: How low can we go?," *Invest. Radiol.*, vol. 47, no. 8, pp. 468–474, 2012.

[30] Y. Yamada, M. Jinzaki, Y. Tanami, E. Shiomi, H. Sugiura, T. Abe, and S. Kuribayashi, "Model-based iterative reconstruction technique for ultralow-dose computed tomography of the lung: A pilot study," *Invest. Radiol.*, vol. 47, no. 8, pp. 482–489, 2012.

[31] P. J. Pickhardt, M. G. Lubner, D. H. Kim, J. Tang, J. A. Ruma, A. M. del Rio, and G.-H. Chen, "Abdominal CT with model-based iterative reconstruction (MBIR): Initial results of a prospective trial comparing ultralow-dose with standard-dose imaging," *Am. J. Roentgenol.*, vol. 199, pp. 1266–1274, 2012.

[32] P. Sukovic and N. H. Clinthorne, "Penalized weighted least-squares image reconstruction for dual energy x-ray transmission tomography," *IEEE Trans. Med. Imag.*, vol. 19, no. 11, pp. 1075–1081, Nov. 2000.

[33] J. A. Fessler, I. Elbakri, P. Sukovic, and N. H. Clinthorn, "Maximum-likelihood dual-energy tomographic image reconstruction," in *Proc. SPIE Med. Imag.: Image Process.*, 2002, pp. 38–49.

[34] J. A. O'Sullivan and J. Benac, "Alternating minimization algorithms for transmission tomography," *IEEE Trans. Med. Imag.*, vol. 26, no. 3, pp. 283–297, Mar. 2007.

[35] W. Huh and J. A. Fessler, "Model-based image reconstruction for dual-energy X-ray CT with fast KVP switching," in *Proc. IEEE Int. Symp. Biomed. Imag.: From Nano to Macro*, 2009, pp. 326–329.

[36] O. Semerci and E. L. Miller, "A parametric level-set approach to simultaneous object identification and background reconstruction for dual-energy computed tomography," *IEEE Trans. Image Process.*, vol. 21, no. 5, pp. 2719–2734, May 2012.

[37] P. E. Kinahan, J. A. Fessler, A. M. Alessio, and T. K. Lewellen, "Quantative attenuation correction for PET/CT using iterative reconstruction of low-dose dual-energy CT," in *Proc. IEEE Nucl. Sci. Symp.*, 2004, vol. 5, pp. 3285–3289.

[38] P. E. Kinahan, A. M. Alessio, and J. A. Fessler, "Dual energy CT attenuation correction methods for quantitative assessment of response to cancer therapy with PET/CT imaging," *Technol. Cancer Res. Treatment*, vol. 5, no. 4, pp. 319–327, Aug. 2006.

[39] W. Huh and J. A. Fessler, "Iterative image reconstruction for dual-energy x-ray CT using regularized material sinogram estimates," in *Proc. IEEE Int. Symp. Biomed. Imag.: From Nano to Macro*, 2011, pp. 1512–1515.

[40] R. Alvarez and E. Seppi, "A comparison of noise and dose in conventional and energy selective computed tomography," *IEEE Trans. Nucl. Sci.*, vol. 26, pp. 2853–2856, Apr. 1979.

[41] W. A. Kalender, E. Klotz, and L. Kostaridou, "An algorithm for noise suppression in dual energy CT material density images," *IEEE Trans. Med. Imag.*, vol. 7, no. 3, pp. 218–224, Sep. 1988.

[42] R. Zhang, J.-B. Thibault, C. A. Bouman, K. D. Sauer, and J. Hsieh, "A model-based iterative algorithm for dual-energy X-ray CT reconstruction," in *Proc. 2nd Int. Meet. Image Format. X-Ray CT*, 2012, pp. 439–443.

[43] N. H. Clinthorne, "A constrained dual-energy reconstruction method for material-selective transmission tomography," *Nucl. Instrum. Methods Phys. Res. A*, vol. 353, no. 1–3, pp. 347–348, 1994.

[44] J.-B. Thibault, C. A. Bouman, K. D. Sauer, and J. Hsieh, "A recursive filter for noise reduction in statistical tomographic imaging," in *Proc. SPIE Computat. Imag. IV*, 2006, p. 60650X.

[45] B. De Man and S. Basu, "Distance-driven projection and back projection in three-dimensions," *Phys. Med. Biol.*, vol. 49, no. 11, pp. 2463–2475, Jun. 2004.

[46] A. J. Coleman and M. Sinclair, "A beam-hardening correction using dual-energy computed tomography," *Phys. Med. Biol.*, vol. 30, no. 11, pp. 1251–1256, 1985.

[47] P. Jin, E. Haneda, C. A. Bouman, and K. D. Sauer, "A model-based 3-D multi-slice helical CT reconstruction algorithm for transportation security application," in *Proc. 2nd Int. Meet. Image Format. X-Ray CT*, 2012, pp. 297–300.

[48] S. J. Kisner, E. Haneda, C. A. Bouman, S. Skatter, M. Kourinny, and S. Bedford, "Limited view angle iterative CT reconstruction," in *Proc. SPIE Computat. Imag. X*, 2012, p. 82960F.

[49] S. V. Venkatakrishnan, L. F. Drummy, M. Jackson, M. De Graef, J. Simmons, and C. A. Bouman, "A model based iterative reconstruction algorithm for high angle annular dark field—Scanning transmission electron microscope (HAADF-STEM) tomography," *IEEE Trans. Image Process.*, vol. 22, no. 11, pp. 4532–4544, Nov. 2013.

[50] C. A. Bouman and K. D. Sauer, "A generalized Gaussian image model for edge-preserving MAP estimation," *IEEE Trans. Image Process.*, vol. 2, no. 3, pp. 296–310, Jul. 1993.

[51] Z. Yu, J.-B. Thibault, K. D. Sauer, C. A. Bouman, and J. Hsieh, "Accelerated line search for coordinate descent optimization," in *Proc. IEEE Nucl. Sci. Symp.*, 2006, vol. 5, pp. 2841–2844.

[52] J. Zheng, S. S. Saquib, K. D. Sauer, and C. A. Bouman, "Parallelizable Bayesian tomography algorithms with rapid, guaranteed convergence," *IEEE Trans. Image Process.*, vol. 9, no. 10, pp. 1745–1759, Oct. 2000.

[53] H. Erdogan and J. A. Fessler, "Monotonic algorithms for transmission tomography," *IEEE Trans. Med. Imag.*, vol. 18, no. 9, pp. 801–814, Sep. 1999.

[54] J. A. Fessler and A. O. Hero, "Penalized maximum-likelihood image reconstruction using space-alternating generalized EM algorithms," *IEEE Trans. Image Process.*, vol. 4, no. 10, pp. 1417–1429, Oct. 1995.

[55] E. K. P. Chong and S. H. Żak, *An Introduction to Optimization Methods*, 3rd ed. New York: Wiley, 2008, ch. 20.

[56] D. H. Martin, "The essence of invexity," *J. Optim. Theory Appl.*, vol. 47, no. 1, pp. 65–76, Sep. 1985.

[57] X. Wu, J. W. Leblanc, and P. Sainath, "Method for calibrating a dual-spectral computed tomography (CT) system," U.S. Patent 7 801 264, Sep. 21, 2010.

[58] X. Wu, D. A. Langan, D. Xu, T. M. Benson, J. D. Pack, A. M. Schmitz, J. E. Tkaczyk, J. Leverentz, and P. Licato, "Monochromatic CT image representation via fast switching dual kVp," in *Proc. SPIE Med. Imag.: Phys. Med. Imag.*, 2009, p. 725845.

[59] C. J. Bischof and J. C. Ehrhardt, "Modulation transfer function of the EMI CT head scanner," *Med. Phys.*, vol. 4, no. 2, pp. 163–167, 1977.

[60] R. T. Droege and R. L. Morin, "A practical method to measure the MTF of CT scanners," *Med. Phys.*, vol. 9, no. 5, pp. 758–760, 1982.